iScience

CellPress

Article

Biomechanics of Endothelial Tubule Formation Differentially Modulated by Cerebral Cavernous Malformation Proteins

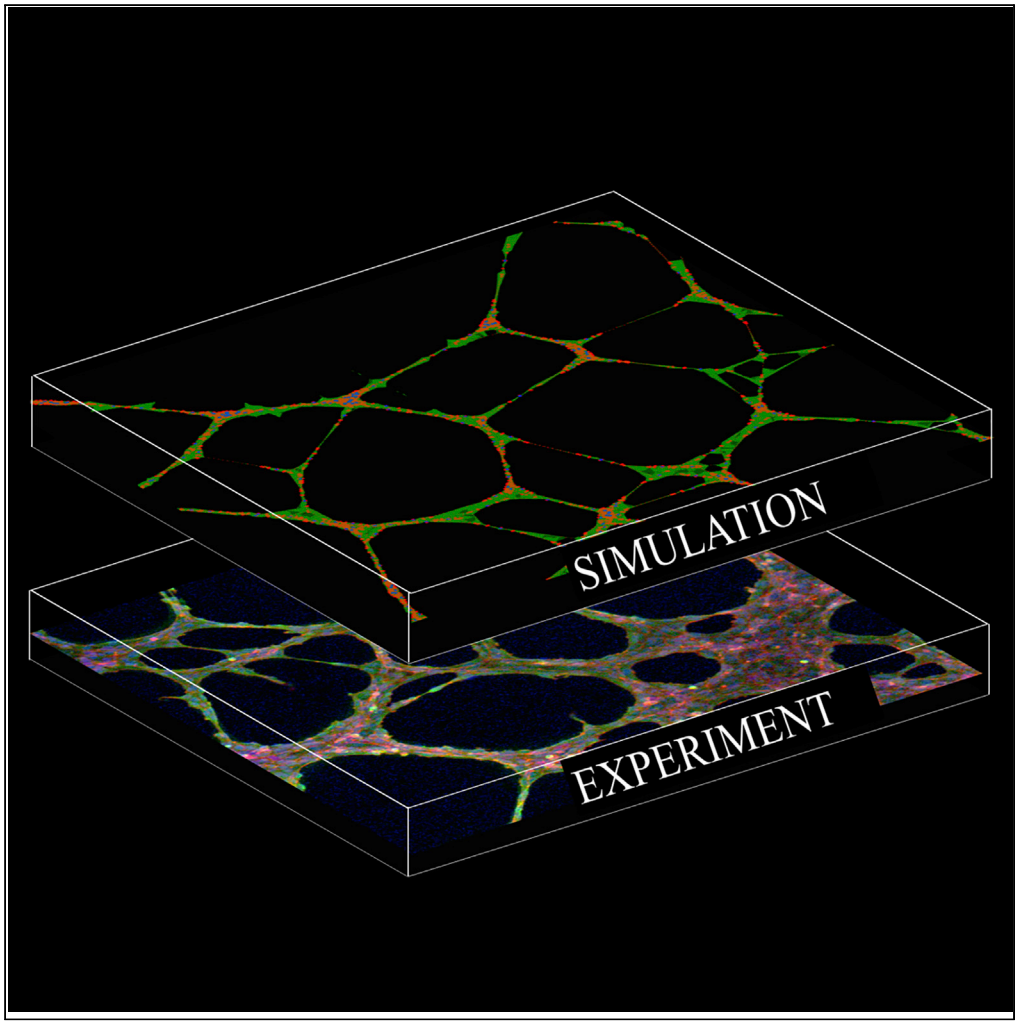

Olga Chernaya, Anastasia Zhurikhina, Siarhei Hladyshau, ..., Vaishnavi Andra, Todd A. Sulchek, Denis Tsygankov

denis.tsygankov@bme.gatech.edu

HIGHLIGHTS

A biophysical model reveals the differential effects of CCM proteins on cell behavior

CCM proteins are critical for the balance of cell-cell and cell-matrix interactions

Altered cell biomechanics explains the limited phenotype rescue by ROCK inhibition

Knockdown of CCM3 expression leads to unique defects in the actomyosin organization

Chernaya et al., iScience 9, 347–358
November 30, 2018
https://doi.org/10.1016/j.isci.2018.11.001

iScience

CellPress

Article

Biomechanics of Endothelial Tubule Formation Differentially Modulated by Cerebral Cavernous Malformation Proteins

Olga Chernaya,[1,3] Anastasia Zhurikhina,[1,3] Siarhei Hladyshau,[1] William Pilcher,[1] Katherine M. Young,[1] Jillian Ortner,[1] Vaishnavi Andra,[1] Todd A. Sulchek,[2] and Denis Tsygankov[1,4,*]

SUMMARY

At early stages of organismal development, endothelial cells self-organize into complex networks subsequently giving rise to mature blood vessels. The compromised collective behavior of endothelial cells leads to the development of a number of vascular diseases, many of which can be life-threatening. Cerebral cavernous malformation is an example of vascular diseases caused by abnormal development of blood vessels in the brain. Despite numerous efforts to date, enlarged blood vessels (cavernomas) can be effectively treated only by risky and complex brain surgery. In this work, we use a comprehensive simulation model to dissect the mechanisms contributing to an emergent behavior of the multicellular system. By tightly integrating computational and experimental approaches we gain a systems-level understanding of the basic mechanisms of vascular tubule formation, its destabilization, and pharmacological rescue, which may facilitate the development of new strategies for manipulating collective endothelial cell behavior in the disease context.

INTRODUCTION

Collective cell behavior is a hallmark of organismal development, tissue regeneration, and disease progression. Among the most illustrious examples of this phenomenon are collective cell migration, which underlies embryonic development (Scarpa and Mayor, 2016) and cancer spreading (Mayor and Etienne-Manneville, 2016), and multicellular self-organization at the early stages of embryogenesis, when groups of vascular precursor cells give rise to the vascular tree (Betz et al., 2016). Coordinated behavior in multicellular clusters is dependent on the characteristics of individual cells, their active communication with neighbors, and interactions with the extracellular matrix (ECM).

When studying collective cell behavior, understanding the complex interplay of multiple parameters that change simultaneously across different spatial and temporal scales often requires computational modeling. Indeed, conceptual models and verbal reasoning cannot predict the behavior of complex systems with many interacting components. In contrast, holistic simulations models informed and validated by experimental data enable systems-level analysis through the predict-test-refine cycle. Here we designed a simulation model that explicitly incorporates cytoskeletal stiffness and protrusive activity of individual cells, as well as forces developed through cell-cell and cell-matrix interactions, into the morphodynamic context. Using this model, we gain insights into the emergence of multicellular structures at the initial stages of vasculogenesis and establish the effects of CCM protein deficiency on the integrity of the endothelial tubule networks.

Cerebral cavernous malformations (CCMs) are common vascular lesions that predispose affected individuals to brain hemorrhage. CCM disease is characterized by the presence of aberrantly enlarged "cavernous" endothelial channels found exclusively in the central nervous system. Genetic studies identified that CCMs result from homozygous inactivating mutations in one of three genes, *krit1 (ccm1), ccm2, or pdcd10 (ccm3)* (Pagenstecher et al., 2009). Products of these genes, CCM proteins, form a complex involved in the regulation of cytoskeletal dynamics through controlling RhoA function (Fischer et al., 2013). An increase in RhoA activity is a signature feature of CCM lesions at the molecular level. It was shown that pharmacological inhibition of RhoA decreases vascular permeability, improves vascular stability *in vitro* and *in vivo*, and decreases the number of lesions in KRIT1- and CCM2-deficient animals (Borikova et al., 2010; Stockton et al., 2010; McDonald et al., 2012).

[1]Wallace H. Coulter Department of Biomedical Engineering, Georgia Institute of Technology and Emory University School of Medicine, Atlanta, GA 30332, USA

[2]George W. Woodruff School of Mechanical Engineering, Georgia Institute of Technology, Atlanta, GA 30332, USA

[3]These authors contributed equally

[4]Lead Contact

*Correspondence: denis.tsygankov@bme.gatech.edu

https://doi.org/10.1016/j.isci.2018.11.001

Several studies identified additional mechanisms contributing to the development of CCM, such as endothelial-to-mesenchymal transition (Maddaluno et al., 2013), down-regulation of Notch signaling (Schulz et al., 2015), and KLF4 signaling (Zhou et al., 2016). Although dysregulation of RhoA activity appears central for disease development, an increasing volume of evidence indicates that, in addition to forming a complex that controls RhoA, CCM proteins have non-overlapping functions (Fisher and Boggon, 2014). These independent characteristics of KRTI1, CCM2, and PDCD10 may explain documented differences in clinical phenotypes caused by mutations in either of the genes (Shenkar et al., 2015). Recently it has been proposed that loss of KRIT1, CCM2, or PDCD10 gives rise to tubular structures with unique phenotypes, which are attributed not only to increased cellular stiffness but also to an imbalance of cell-cell (on PDCD10 loss) or cell-ECM adhesion (on KRIT1 loss) (Beltran et al., 2018).

Here, by using an integrative approach that couples computational modeling and experimental characterization, we report the biomechanical factors that contribute to the observed CCM phenotypes and its limited rescue by ROCK inhibition, which further expands our understanding of non-overlapping functions of *ccm* genes and advances the general knowledge of vascular tubule formation.

RESULTS

Inhibition of ROCK Does Not Fully Restore Endothelial Tubule Formation in Cells with CCM Expression Knockdown

Knockdown of either of CCM protein expression disrupts endothelial tubule formation on Matrigel (Borikova et al., 2010). In addition, previous studies indicated that inhibiting ROCK function effectively increases mean tubule length thus restoring vascular networks in endothelial cell cultures with knockdown of CCM protein expression (Borikova et al., 2010). However, the visual appearance of cellular structures on pharmacological inhibition of ROCK activity by H1152 does *not* closely resemble the wild-type (WT) patterns. Here, we aimed to quantitatively evaluate this difference in the patterns of treated and untreated endothelial cells with and without CCM knockdown. To this end, we transduced HUVEC cells with lentiviral particles carrying shRNAs or transfected them with siRNA against *krit1, ccm2, and pdcd10* genes (see Figure S1) before plating on an 800-μm-thick layer of Matrigel.

Consistent with previously published work, tubule patterns generated by either of the CCM protein KD cells were distinct from those in WT cultures and could be easily distinguished from each other (Figure 1A, *top panels*). As expected, treatment with H1152 resulted in a partial rescue of vascular networks of KD cells (Figure 1A, *lower panels*).

To obtain quantitative measures of the differences between the CCM knockdown tubule patterns, and a degree of "rescue" in ROCK inhibitor treated cultures, we performed morphometric analysis of tubules formed in the absence or presence of H1152 in the media at the time of cell plating. The measurements included the void area, the number of background pixels corresponding to the area of the substrate not covered by cells, and the mean loop count, the number of isolated regions in the dish enclosed by cells (Figure 1B).

Quantitative analysis showed that all CCM knockdown cultures had a significantly increased void area, as compared with WT endothelial cell (EC) tubules (Table S1). For KRIT1 and PDCD10 knockdown cultures, void areas were approximately 10% larger and CCM2 approximately 5% larger than in WT cultures. The mean loop count was significantly decreased for KRIT1 ($p < 0.01$) and PDCD10 ($p < 0.01$) but not for CCM2 ($p = 0.21$). KRIT1 cultures had 75% fewer loops on average compared with WT cultures, whereas PDCD10 failed to form tubule networks.

On treatment with H1152, all CCM knockdowns showed significant differences with respect to their untreated cultures, with a trend toward WT tubule pattern. This includes a lower void area and a higher loop count. However, even though the void area in KRIT1 KD and PDCD10 KD cultures treated by the ROCK inhibitor is "rescued" (no significant difference from WT), the loop count in these KDs remains significantly different from that of untreated WT (Figure 1B).

These results might be explained by two factors: (1) the increased ROCK activity in CCM KD cells contributes to but does not fully explain the phenotypes of vascular tubule patterns generated by CCM KD cells and (2) pharmacological inhibition of ROCK activity imposes additional biomechanical perturbations on cell

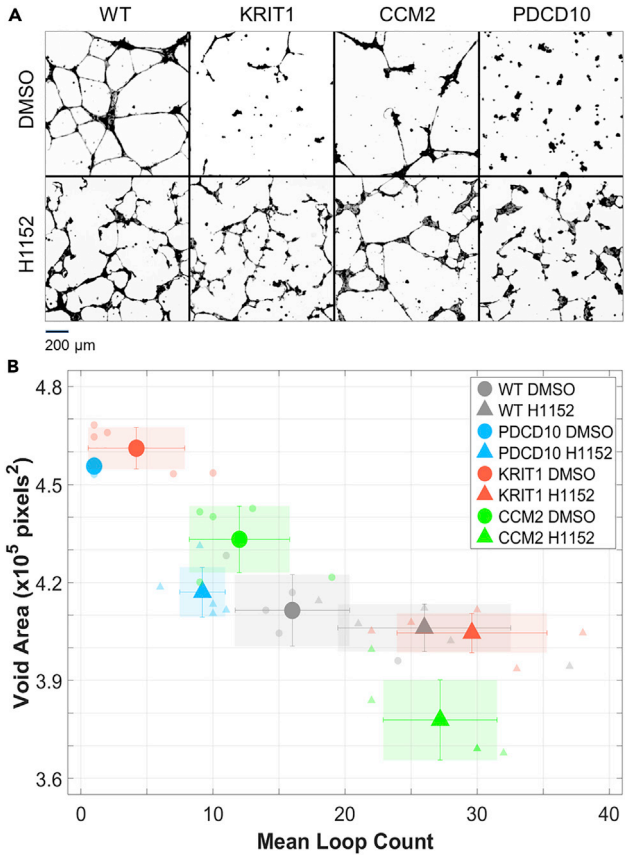

Figure 1. Inhibition of Rho Kinase Leads to Incomplete Rescue of Vascular Tubule Defects in Endothelial Cell Cultures with Loss of KRIT1, CCM2, and PDCD10

(A) Representative images of vascular tubules generated by HUVEC cells infected with control PLKO.1 (WT) or shRNA carrying lentiviral particles (see also Figure S1). Cells with knockdown of KRIT1, CCM2, or PDCD10 expression were plated on growth factor-reduced Matrigel in the presence or absence of 1 μM of H1152, fixed at 18 hr after plating, and stained with rhodamine-phalloidin to visualize actin cytoskeleton.

(B) Results of morphometric analysis of the tubule network integrity. Void area (in pixels) measures the area of the plate not covered by cells. Mean loop count measures the number of background regions enclosed by interconnected cells. When considering both measures, all knockdown cultures and all treatment cultures are significantly different from WT cultures ($p < 0.05$). Data are represented as mean $\pm 2 \cdot$SEM.

behavior, resulting in a significant change of both WT and CCM KD pattern, such as, for example, a suboptimal level of cytoskeletal tension required for efficient vascular network development. To investigate which of the potential factors could plausibly explain our findings, we turned to computational modeling.

Computational Modeling Links EC Biomechanics to Disrupted Tubule Patterns in CCM KD Cells and Incomplete Rescue upon ROCK Inhibition

Our model is designed to explicitly account for protrusive activity, cytoskeletal stiffness, and forces developed through cell interactions. For this work, we developed a three-dimensional simulation model that differs from our previously reported two-dimensional cell model design in several critically important aspects. First, we model cell-ECM interaction explicitly through the extension of cell protrusions and establishment of elastic contacts within the 3D substrate, as opposed to the viscous drag interaction between a cell and the substrate surface in the old model. Second, even with the fixed total volume, the *ellipsoidal* cell body allows the cell to stretch and spread on the substrate due to lateral cell-cell interactions. Previously, the fixed area of the *elliptical* cell body would allow cells to stretch but not spread. Finally, in contrast to the old model, here we introduce a (presumably substrate-mediated) long-distance sensing between plated cells during their directed protrusion extension toward each other. This change was necessary for achieving close correspondence between the simulated and the experimentally

observed dynamics at the cellular level (see Figures S2–S4). Indeed, human umbilical vein endothelial cells (HUVECs) with an average diameter of 17.21 $\pm$ 2.13 μm are surprisingly efficient at reaching each other by extending protrusions from distances as long as 120 μm (Video S1).

We choose to represent the body of each endothelial cell as an extendable ellipsoid (Figure 2A) with viscoelastic axes to account for cell stiffness while maintaining high efficiency of simulations with thousands of interacting cells. Each cell interacts with the other cells by mechanosensitive lateral protrusions, initiated radially from the edge of the cell body in the *xy*-plane and forming attachments (cell-cell contacts) on reaching cell bodies of other cells (see Figures S2 and S3). The protrusions function in two distinct modes. In the "extending" mode, protrusions extend with a rate u_{prot} (0.017 μm/s) toward other cells. If the distance between the centers of two cells, R, is such that $R_{short} < R < R_{long}$, the protrusions extended by the cell are labeled as long range. Each cell has a limit on the maximum number of long-range protrusions at any given time, $N_{long} \leq 5$, whereas short-range protrusions extend toward the cells at close proximity $R < R_{short}$ (see Figure S4). On reaching the body of another cell, both types of protrusions switch to the "pulling" mode and begin to retract with a rate u_{retr} (0.003 μm/s). If the distance between the centers of two cells connected by a retracting long-range protrusion becomes less than R_{short}, this protrusion is automatically relabeled as short range, so that new long-range protrusions can be initiated and the total number of protrusions per cell, $N_{total} = N_{long} + N_{short}$, can increase. However, new short-range protrusions are not *initiated* if $N_{total} > N_{lim} = 15$. This setup ensures that there is a limit on how many protrusions a given cell can initiate at any given time while allowing for initiating new long-range interactions after the retraction of previously initiated protrusions is completed. Because cell-cell contacts in the model are defined as an attachment of a protrusion to another cell's body, we do not take into consideration interactions (or collisions) between different protrusions. In addition to lateral interactions between each other, cells also interact with the ECM that they are platted on. In the model, vertically directed protrusions establish cell-ECM contacts on reaching a length R_{bott}. Up to N_{bott} contacts per cell can be formed. Each of the above-mentioned parameters (see Table S2) has been adjusted through simulation scans to closely reproduce WT cell dynamics observed in our live imaging experiments.

The cell-cell and cell-ECM contacts were modeled as elastic springs with spring constant k_{pull}. By extending these springs, cells exert contractile forces on each other, which ultimately leads to the emergence of a multicellular pattern (a network of connected cells). To model contact breakage events, we assumed that each contact spring has a finite extension-dependent probability, $P_{cell-cell} = 1 - \exp\left(-\frac{l^2}{k_{lat}^2}\right)$, of being removed, so that the corresponding protrusion can switch back to the extending mode. The parameter regulating the breakage probability is effectively an indicator of the cell-cell adhesion strength. Similarly, the breakage of the contacts between endothelial cells and the ECM, $P_{cell-ecm} = 1 - \exp\left(-\frac{l^2}{k_{bott}^2}\right)$, defines the resistance of the cell to lateral displacement under external forces and, thus, represents the cell-ECM adhesion strength. On the timescale of the tube formation, we can assume that ECs are not motile by themselves and move only through the interactions with other cells.

The state of the system is defined by (1) the location $\{x,y\}$, orientation $\{\varphi\}$, and deformation $\left\{a, b, c = \frac{3V}{4\pi ab}\right\}$ of each cell body with a constant volume V; (2) the status (attached or detached) and the length L of each protrusion; (3) the length l of each contact spring; and (4) an additional variable $\{\xi\}$, which defines the orientation of uniformly distributed lateral protrusion bases on the cell body with respect to the orientation of the semi-principle axes in the horizontal plane. The latter is needed for the proper reorientation of the cell body with respect to the direction of forces acting on it. This ensures very realistic deformation of the simplified geometry of the cell under mechanical stresses. At each time step, the set of coordinates $i = \{x,y,\varphi,a,b,\xi\}$ is updated according to the force balance along each of the coordinates: $F_i = -\eta_i \nu_i - \nabla_i H = 0$, where η_i and ν_i are the viscous drag and the rate of change of the coordinate i. For example, the change in cell body orientation is found as $\varphi(t + \Delta t) = \varphi(t) - \frac{\Delta t}{\eta_\varphi}\frac{\partial H}{\partial \varphi}$, where H is the total Hamiltonian of the system, which includes all elastic components from the cell bodies and contact springs. The variables L and l are updated according to the status of each protrusion at each time step. Collectively these steps lead to the evolution of the system and the emergence of the multicellular patterns.

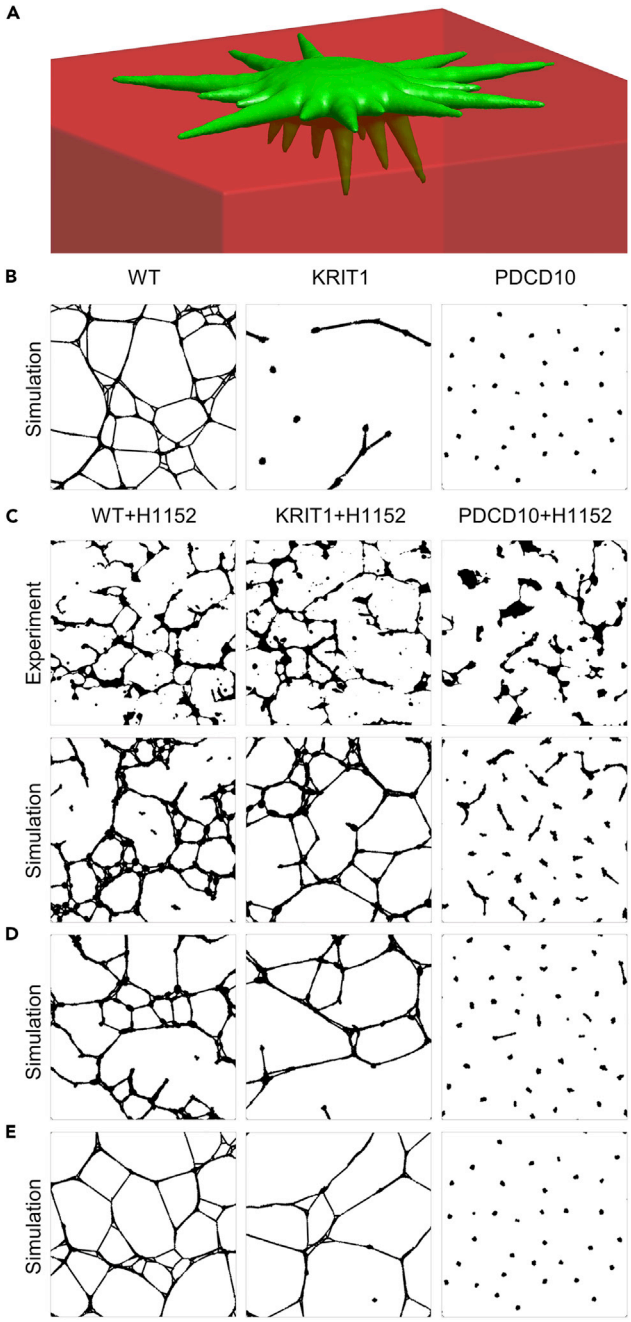

Figure 2. Simulations of Endothelial Tube Formation by WT and CCM KD Cells Untreated and Treated with the ROCK Inhibitor H1152

(A) An illustration of the cell model with an ellipsoidal cell body, mechanosensitive lateral protrusion responsible for cell-cell interactions, and downward-directed protrusions responsible for cell-ECM interactions (see also Figures S2–S4).

(B) Simulated cell formations that reproduce experimental patterns of untreated cells in the top row of Figure 1A (see also Figure S5).

(C) Comparison of experimental images (top row) and simulated multicellular formations (bottom row) of H1152-treated cells (see also Figures S6–S8).

(D) Simulated patterns resulted from the same k_{lat} and k_{bott} as in B, but with the decreased cytoskeletal stiffness, pulling force, and the range of cell-cell sensing.

(E) Simulated patterns resulting from an adjustment (partial rescue) of only the phenotype-defining parameters k_{lat} and k_{bott}.

First, we used this model to establish the parameters that are responsible for the CCM phenotype. KRIT1 and PDCD10 KD cells form characteristic, easily distinguishable patterns, whereas the CCM2 phenotype appears to be less pronounced, being closer to the WT in terms of both the void area and the hole count measures (Figure 1A). Thus, for modeling purposes, we focused on the analysis of KRIT1 and PDCD10 patterns. Consistent with the previous work (Beltran et al., 2018), the 3D cell model readily reproduces a highly interconnected mesh in WT, elongated and branching but disconnected fragments in KRIT1, and round isolated cell clusters in PDCD10 by properly adjusting the stability/strength of cell-ECM and cell-cell contacts (Figures 2B and S5). Because our live cell imaging never showed a single event of cell-cell contact breakage in WT, we set the probability of breakage for WT cells to zero ($k_{lat} = \infty$). For the KRIT1 cells, the breakage probability is small but finite ($k_{lat} = 6000$ μm), whereas for the PDCD10 cells, the breakage probability is high ($k_{lat} = 300$ μm). In contrast, the resistance to the lateral forces due to cell-ECM attachments is low in KRIT1 ($k_{bott} = 5$ μm) and high in PDCD10 ($k_{bott} = 20$ μm).

Next, we sought to reproduce the patterns of WT, KRIT1, and PDCD10 cells treated by the ROCK inhibitor H1152. An extensive set of simulation scans systematically exploring multiple model parameters (Figures S6–S8) allowed us to successfully reproduce the experimentally observed cell formations (Figure 2C). This close correspondence was achieved by adjusting the parameters in the following way: (1) the stability of cell-cell contacts was increased 2-fold ($k_{lat} = \infty$ for WT, $k_{lat} = 12{,}000$ μm for KRIT1, $k_{lat} = 600$ μm for PDCD10); (2) the stability of cell-ECM contacts was also increased 2-fold ($k_{bott} = 40$ for WT, $k_{bott} = 10$ μm for KRIT1, $k_{bott} = 40$ μm for PDCD10); (3) the cytoskeletal stiffness was reduced from $k_{xy} = 5$ and $k_z = 100$ to $k_{xy} = 1$ and $k_z = 1$ before and after treatment, respectively; (4) the pulling force resulting from the extension of the contact spring was decreased, changing the spring constant from $k_{pull} = 0.5$ to $k_{pull} = 0.1$; (5) the cell-sensing distance reduced from $R_{long} = 120\,\mu m$ and $R_{short} = 40$ μm to $R_{long} = 95$ μm and $R_{short} = 30$ μm. The convergence toward these parameter values suggests that not only the phenotype-defining parameters k_{lat} and k_{bott} but also the parameters associated with the cytoskeletal stiffness, protrusion contractility, and the range of cell-cell sensing (presumably due to a reduced contraction of the Matrigel) are responsible for the specific arrangement of WT and CCM KD cells in tubular structures on the treatment with the ROCK inhibitor.

For the "control," we ran simulations with the same parameters as earlier except for the phenotype-defining parameters k_{lat} and k_{bott}, which we kept as in Figure 2B. The resulting patterns (Figure 2D) are not consistent with the experimental images, indicating that the change in cytoskeletal stiffness, protrusion contractility, and the range of cell-cell sensing is not exclusively responsible for the observed effects of ROCK inhibition. Therefore, our simulation results argue that the rescue still takes place, although to a limited degree.

In another important "control simulation," we set the phenotype-defining parameters k_{lat} and k_{bott} to the partially rescued values as in Figure 2B and left the other parameters unchanged. Again, the resulting patterns (Figure 2E) clearly deviate from the experimental images. This discrepancy justifies the need for careful considerations of the secondary, off-target effects of the perturbation of RhoA signaling in the CCM-deficient cells. This result emphasizes the critical importance of the holistic modeling approaches, which accounts for multiple factors that could be potentially affected by a pharmacological treatment targeting a key cell-signaling molecule, such as ROCK.

To confirm the model predictions regarding the modulation of cell-cell and cell-ECM interaction in conjunction with the alterations of the contractile characteristics of the CCM KD cells, we turn back to the experimental characterization, now focusing on the cell stiffness and the gene expression profiles.

Knockdown of CCM Protein Expression Leads to Changes in Actomyosin Architecture and Increases the Cellular Stiffness of KRIT1 and CCM2 but Not PDCD10 KD Cells

Despite growing evidence of unique features of KRIT1, CCM2, and PDCD10 knockdown phenotypes in human disease (Fischer et al., 2013; Fisher and Boggon, 2014) and *in vitro* (Beltran et al., 2018), and multiple pathways involved in CCM disease progression, RhoA-ROCK activity remains the most extensively characterized signaling pathway responsible for CCM lesions development (Beltran et al., 2018). To date, several pharmacological compounds targeting RhoA signaling are being tested to prevent or reduce the development of CCM lesions in pre-clinical trials (Bond et al., 2015).

According to predictions of the model described earlier, changes in cytoskeletal tension and cellular responses to external forces have a dramatic effect on tubule pattern formation. In the context of CCM KD, increased

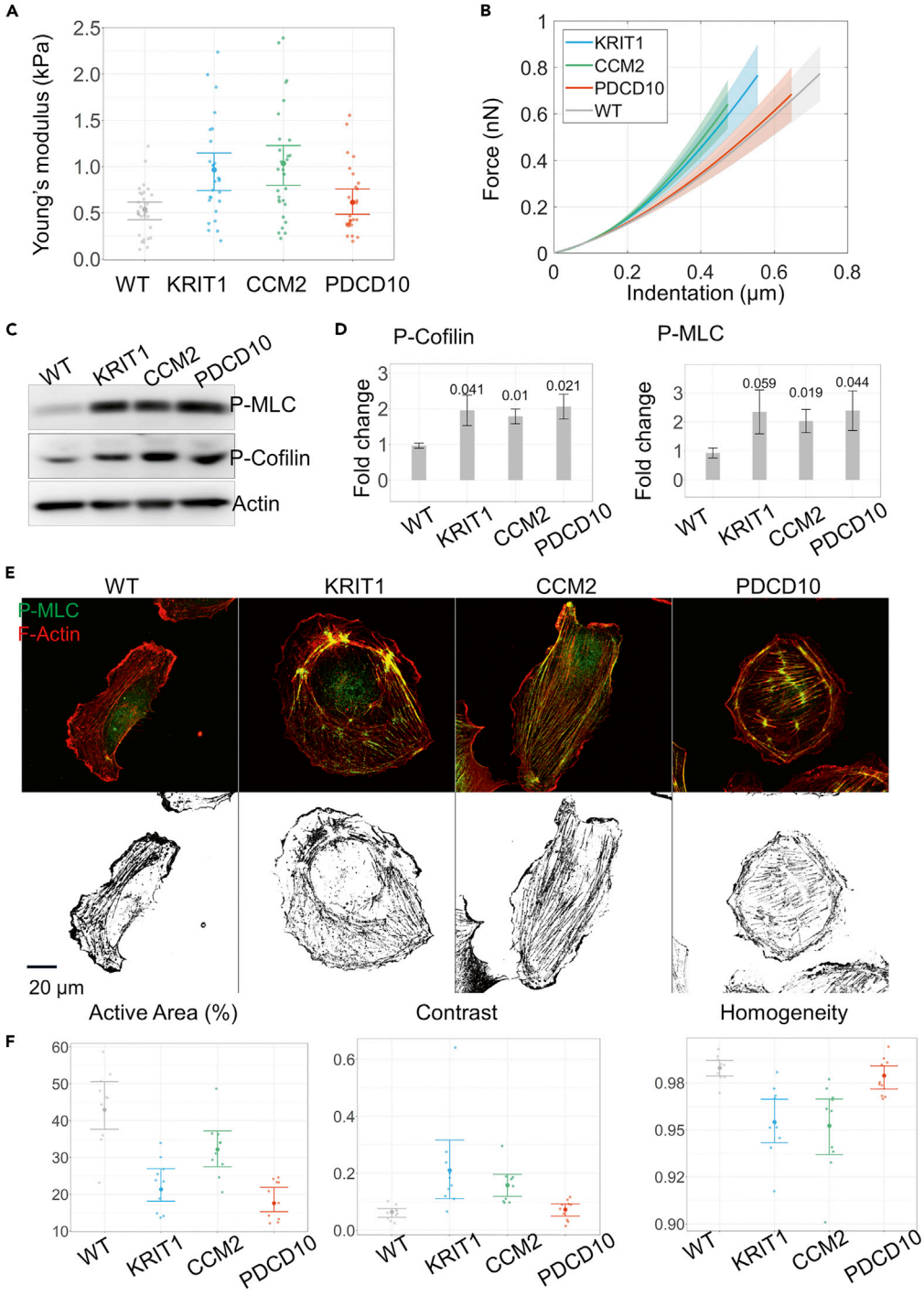

Figure 3. Changes in Actomyosin Cytoskeleton Associated with Loss of CCM Protein Expression Result in Increased Stiffness of Cells with Knockdown of KRIT1 and CCM2 but Not PDCD10

(A) AFM stiffness measurement results for single PLKO.1 (WT) and cells with knockdown of KRIT1, CCM2, and PDCD10. The graph shows mean values and standard deviations of measurements from up to 30 cells in each group. Note higher stiffness of KRIT1 and CCM2 KD but not PDCD10 KD cells when compared with WT. The data shown are from one representative of three independent experiments.

(B) The graph shows representative force curves of WT cells and cells with loss of CCM protein expression recorded by AFM, with shaded area representing $\pm 2 \cdot$SEM.

Figure 3. *Continued*

(C) Representative immunoblot showing increased phosphorylation of myosin light chain (MLC-P) and cofilin in HUVEC cells with loss of KRIT1, CCM2, and PDCD10 expression. Total actin used as a loading control.

(D) Quantification of fold change of MLC-P and phospho-cofilin levels. Optical densities of the corresponding bands were normalized to the loading control; the results represent an increase over PLKO.1 (WT) expression levels (mean ± SEM, n = 3 experiments. In the bar graphs p values are indicated for each of the KD cultures compared with WT).

(E) Upper row: representative images of cells immunolabeled with an antibody against phosphorylated myosin light chain (MLC-P) (*green*), and incubated with rhodamine-phalloidin to visualize F-actin (*red*). Lower row: results of subtraction of thresholded signals from the F-actin and MLC-P channels from the images of cells above.

(F) Percentage of the active area defined here as a fraction of the pixels, which have an over-threshold intensity of the F-actin signal but a sub-threshold intensity of the MLC-P signal, among all pixels within a near-edge strip. Contrast and homogeneity are statistical measures of the image derived from the gray-level co-occurrence matrix (see Transparent Methods). Data are represented as mean ±2·SEM.

cellular stiffness is expected as a consequence of dysregulated RhoA function (Sreenivasappa et al., 2014). Thus, we aimed to directly measure cellular stiffness in CCM KD and compare it with WT cultures.

Atomic force microscopy (AFM) measurements were taken from 30–50 cells in each of the experimental groups at 24 hr after plating. The results of three independent experiments showed significantly higher stiffness of KRIT1 KD ($p = 0.00053$) and CCM2 KD ($p = 0.00014$) cells as compared with WT cells. However, the stiffness of PDCD10 KD cell was not different from that of WT cultures, $p = 0.23$ (Figures 3A and 3B). This was unexpected, because similarly to previously published data (Borikova et al., 2010; Beltran et al., 2018), we did observe statistically significant increase in myosin light chain (MLC) and cofilin phosphorylation in all CCM KD cells (Figures 3C and 3D), thus excluding a possibility that ROCK activity in PDCD10 KD cells was lower than in KRIT1 or CCM2 KD cultures.

Taken together, AFM measurement data demonstrated that, despite activation of a common signaling pathway and comparable increase in MLC and cofilin phosphorylation levels, biomechanical characteristics of the CCM KD cells are far from identical. Thus, a decrease in cell-cell or cell-ECM adhesion predicted by the model cannot be attributed solely to an increased cytoskeletal tension. This is clearly the case for cells with PDCD10 gene knockdown.

We reasoned that unexpectedly low stiffness of PDCD10 cells might be due to specifics of the architecture of actin cytoskeleton in these cells. Indeed, as demonstrated in previous studies, cells with highly aligned stress fibers had lower overall stiffness when compared with cells with a more intertwined organization of the cytoskeleton (Zhou et al., 2017). To address this possibility, we visualized filamentous actin with fluorescently labeled phalloidin and performed immunocytochemical staining of cultures using antibodies against MLC-P (Figure 3E, top row) to study the distribution of actomyosin fibers in WT and KD cells. Consistent with western blotting data (Figures 3C and 3D), the overall intensity of staining of EC cultures with anti-MLC-P antibodies was not different among all types of KD cells. To quantify the distribution of total filamentous actin as well as myosin II-containing contractile fibers in the cortical layer and throughout cytoplasm, we performed two types of analysis: (1) quantification of percent presence of non-bundled F-actin near the cell edge and (2) assessment of the internal structuring of actin bundles using the standard texture measures, contrast and homogeneity, derived from the gray-level signal distribution in cell images (see Transparent Methods). As shown in Figures 3E and 3F, the width of lamellipodia, the cortical layer characterized by high F-actin staining, was higher in WT than in all CCM KD cells (Figure 3E). This area of high F-actin activity was dramatically reduced in PDCD10 KD cells. Analysis of F-actin distribution showed that KRIT1 and CCM2 KD cell cytoskeleton had a higher contrast of actin bundles and was characterized by less homogeneity of staining as compared with WT and PDCD10 KD cells (Figure 3F).

Although elevated RhoA activity is a common feature of CCM KD cells, the overall stiffness and the underlying architecture of actomyosin cytoskeleton are drastically different among CCM KD cultures. The characteristics of actin cytoskeleton organization may contribute to differences in biomechanical properties of KD cells, the patterns of vascular networks, and the response of KD cultures to ROCK inhibition.

Gene Expression Analysis and Functional Assays Confirm Differences in Cell-Cell and Cell-ECM Adhesion in CCM KD Cultures

To test predictions of computational modeling, we studied gene expression profiles of WT and CCM KD cells cultured under 2D and 3D (Matrigel) conditions. We reasoned that expression profiles would change

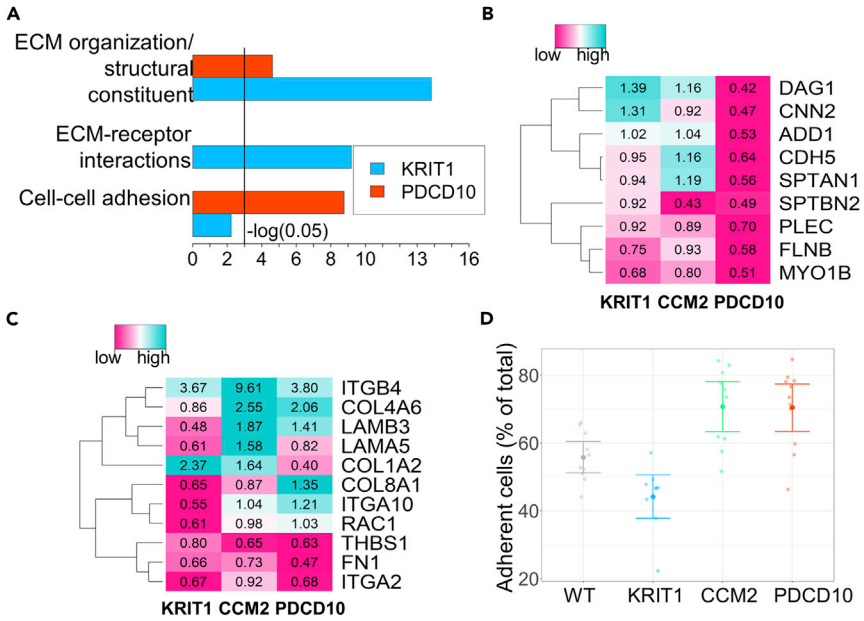

Figure 4. Gene Expression Analysis and Adhesion Assay Reveal Differences in Cell-Cell Adhesion and Cell-ECM Adhesion in CCM KD Cultures

(A) GO term enrichment analysis of selected cellular component gene groups, representing cell-cell and cell-ECM interactions. The graphs show negative log(p values) for KRIT1 KD cells (*blue bars*) and PDCD10 cells (*red bars*) compared with WT cells. Genes associated with ECM interaction (extracellular matrix organization and ECM-receptor interaction) were significantly enriched in cultures lacking KRIT1 expression, whereas genes associated with cell-cell adhesion were over-represented in PDCD10 KD cells (see also Figure S9).

(B) Heatmap of a subset of differentially expressed genes involved in cell-cell adhesion. For a selected set of genes, PDCD10 KD cells showed over-expression in comparison with KRIT1 and CCM2 KD. Text annotation in the heatmap represents fold change of RPKM values in comparison with WT cells (see also Figure S10).

(C) Heatmap of selected differentially expressed genes involved in cell-ECM adhesion.

(D) Adhesion assay demonstrates decreased attachment of KRIT1 KD cells to extracellular matrix. The percentage of adherent cells was quantified as a ratio of absorbance at 590 nm of wells from which non-adherent cells were removed at 30 min after plating.

depending on the length of exposure to Matrigel and performed deep sequencing of RNA collected from cells at the initial (2 hr) as well as late (6 hr) stages of EC tubule formation (see Table S3 for all studied conditions).

Functional enrichment analysis using the DAVID v6.8 bio-informatics resources identified several significantly enriched gene ontology (GO) terms and KEGG pathways genes differentially expressed under specified conditions. Consistent with computational model predictions, enrichment of terms associated with cell-cell adhesion was characteristic of PDCD10 cultures, whereas terms associated with ECM organization and adhesion to ECM were over-represented in KRIT1 KD cultures. The highest enrichment scores were observed for EC tubules at 6 hr after plating on Matrigel (Figures 4 and S9 for full dataset), emphasizing the importance of genes involved in the formation of vascular networks under these conditions.

Detailed analysis of differentially expressed genes identified several sets of genes potentially involved in destabilizing cell-cell adhesion in PDCD10 KD and cell-ECM adhesion in KRIT1 KD cultures (Figure 4, showing the data for 3D culture, 6 hr, and Figure S10 for other studied conditions).

For example, α-adducin, involved in regulating the assembly of actin filaments at the areas of cell-cell contacts, thus stabilizing endothelial barrier (Kugelmann et al., 2015), was significantly decreased in PDCD10 KD cultures across studied culture conditions.

Enrichment of GO terms related to matrix composition and cell-matrix adhesion was higher for KRIT1 KD cultures than for PDCD10 or CCM2 KD cells (Figures 4A and 4C). Although some of the integrin receptor genes and secretory matrix components were down-regulated in KRIT1 KD, expression of other isoforms

was increased (Figures 4A and 4C). To study whether KRIT1 protein KD affects adhesion of cells to the ECM, as suggested by the modeling, we plated cells on the Matrigel-coated surface, allowed them to attach for 30 min, and evaluated the number of adherent cells in WT and CCM protein KD cultures. Among all, KRIT1 KD cells showed the lowest adhesion to the substrate (Figure 4D). This result confirms that loss of KRIT1 expression reduces the strength of cell-ECM interactions.

Consistent with predictions of the computational model, RNA sequencing analysis revealed the differential impairment of cell-cell versus cell-substrate adhesion in KRIT1 and PDCD10 KD endothelial cells.

DISCUSSION

Although RhoA activity has been identified as the key player in the development of CCM (Stockton et al., 2010; Borikova et al., 2010), CCM proteins are involved in other signaling pathways (Maddaluno et al., 2013; Schulz et al., 2015; Zhou et al., 2016; Beltran et al., 2018), creating clear phenotypic differences in the collective behavior of endothelial cells with the knockdown of the different members of the CCM complex: KRIT1, CCM2, and PDCD10. Indeed, in this work, we used direct measurements of cell stiffness and showed that despite significantly elevated phosphorylation of cofilin and MLC in all three knockdowns, only KRIT1 and CCM2 have significantly increased stiffness as compared with the control cells. Subsequent analysis of F-actin distribution offers an explanation of this surprising observation. Our quantitative texture-based image analysis confirmed the visually apparent difference in the spatial arrangement of actin filaments: all three knockdowns show an increased density of actin bundles throughout the cell, but in contrast to KRIT1 and CCM2 KDs, PDCD10 KD cells have shorter and less organized bundles, indicating the lack of the cell-level connectivity of the stress fibers.

This result is important from the pharmacological treatment perspective because targeting the components of the RhoA signaling pathway might rescue the phosphorylation levels of cofilin and MLC but has limited effect on the collective behavior of PDCD10 cells since the overall stiffness of these cells appears not to be the major factor defining their deficient biomechanics. Then, what are the major factors that give rise to the distinct patterns of the collective behavior of CCM KD cells? To address this question, we developed a detailed cell model that explicitly accounts for cell body stiffness and deformation, protrusion-based interactions with the ECM, and the mechanosensitive interaction between the cells initially plated at sub-confluent densities. Our strategy was to relate the biophysical properties of individual cells to the emergent patterns of their collective behavior through the systematic parameter scanning until a close correspondence between the simulated and the experimental images was achieved. Such integrated *in silico/in vitro* experimentation led us to the conclusion that central to the loss of multicellular integrity in KRIT1 and PDCD10 KD cells is the decrease in cell-ECM and cell-cell contact stability, respectively. Our RNA-seq analysis of gene expression is consistent with this result. Although the changes in expression of many genes overlap between KRIT1 and PDCD10 KD cells, GO analysis clearly shows that more genes associated with the ECM re-organization and ECM-receptor interactions are affected by KRIT1 KD, whereas more genes associated with cell-cell adhesion are affected by PDCD10 KD. Furthermore, a more directed assessment of the strength of cell-ECM interaction—the non-adherent cell washout assay—also confirmed the deficiency of the KRIT1 KD cell attachment to Matrigel-coated substrate.

Collectively, these results raise another question: to what degree does normalizing cell signaling downstream of RhoA rescue the interaction of CCM KD cells during the formation of tubular structures? Our ROCK inhibition experiments showed that the patterns of H1152-treated cells are noticeably different from those of the untreated ones. For example, the WT^{H1152} and $KRIT1^{H1152}$ cells form very similar (visually indistinguishable) patterns, but these patterns are very different from the patterns of untreated control cells. Could it be that, although the rescue of cell interactions takes place on H1152 treatment, additional perturbations of cell biomechanics unrelated to the deficiency of CCM proteins continue to affect the resulting endothelial network? Our simulations suggest that both factors play a role. We achieve close correspondence between the simulated and experimental images only if we partially "rescue" the parameters directly affecting the stability of cell-cell and cell-ECM contacts and adjust (perturb) the parameters that affect collective cell behavior through the modulation of stretching and spreading, contractility of protrusions, and the efficiency of long-range cell-cell sensing.

Although this work only scratches the surface of the systems-level understanding of the complex interplay between the regulatory and biomechanical processes during the collective behavior of endothelial cells,

our simulation model provides a platform for further investigation that could take advantage of the integration of genetic and biochemical characterization, quantitative imaging, and systematic predict-test-refine modeling. Many parameters can be involved in the setup of a comprehensive cell model, but focusing on the characterization and experimental verification of the emergent behavior allows us to constrain the range of parameters and gain mechanistic insight as we did in this paper.

Limitations of the Study

The two main measures used for quantitative comparison of experimental and simulated cellular patterns in this study, the void area and the mean loop count, capture the significant variations in the structure of cell formations. However, accounting for subtle but still important geometric features, such as the curvature of the bridges or the variation in their thickness, requires a more comprehensive characterization of complex and diverse cellular patterns. Such a methodology is currently under development.

METHODS

All methods can be found in the accompanying Transparent Methods supplemental file.

DATA AND SOFTWARE AVAILABILITY

The accession number for the sequencing data reported in this paper is GEO: GSE116323.

SUPPLEMENTAL INFORMATION

Supplemental Information includes Transparent Methods, 10 figures, 3 tables, and 1 video and can be found with this article online at https://doi.org/10.1016/j.isci.2018.11.001.

ACKNOWLEDGMENTS

We thank Adriana Beltran for the gift of lentiviral vectors carrying shRNAs against *krit1*, *ccm2*, and *pdcd10*. We also thank Drs. Timothy C. Elston and Gary L. Johnson for their immense support, stimulating discussions, and the ideas regarding the design of this project. We wish to acknowledge the core facilities at the Parker H. Petit Institute for Bioengineering and Bioscience at the Georgia Institute of Technology for the use of their shared equipment, services, and expertise. This work was supported by the U.S. Army Research Office (ARO) grant W911NF-17-1-0395 to D.T. and by funds from the Marcus Foundation, The Georgia Research Alliance, and the Georgia Tech Foundation through their support of the Marcus Center for Therapeutic Cell Characterization and Manufacturing (MC3M) at Georgia Tech.

AUTHOR CONTRIBUTIONS

D.T. designed the computational and experimental studies, analyzed imaging data, and wrote the paper. O.C. performed the majority of experiments and wrote the paper. A.Z. developed the model, performed simulations, and edited the paper; S.H. analyzed RNA-seq data; W.P. analyzed images of cell patterns and edited the paper; K.Y. performed AFM experiments and edited the paper; J.O. and V.A. assisted in AFM data acquisition; T.A.S. provided resources and supervision of AFM experiments.

DECLARATION OF INTERESTS

The authors declare no competing interests.

Received: June 26, 2018
Revised: October 12, 2018
Accepted: October 31, 2018
Published: November 30, 2018

REFERENCES

Beltran, A.S., Olivares-Quintero, J.F., Tsygankov, D., Richardson, B.T., Dibble, C.F., Borikova, A.L., Miller, C.R., Zawistowski, J.S., Sciaky, N., Licea, A.F., et al. (2018). Cerebral cavernous malformation proteins and mekk3 coordinately modulate SMURF1 abundance to control RhoA-dependent endothelial cell phenotypic state. Dev. Cell, [submitted].

Betz, C., Lenard, A., Belting, H.G., and Affolter, M. (2016). Cell behaviors and dynamics during angiogenesis. Development *143*, 2249–2260.

Bond, L.M., Sellers, J.R., and Mckerracher, L. (2015). Rho kinase as a target for cerebral vascular disorders. Future Med. Chem. *7*, 1039–1053.

Borikova, A.L., Dibble, C.F., Sciaky, N., Welch, C.M., Abell, A.N., Bencharit, S., and Johnson, G.L. (2010). Rho kinase inhibition rescues the

endothelial cell cerebral cavernous malformation phenotype. J. Biol. Chem. *285*, 11760–11764.

Fischer, A., Zalvide, J., Faurobert, E., Albiges-Rizo, C., and Tournier-Lasserve, E. (2013). Cerebral cavernous malformations: from CCM genes to endothelial cell homeostasis. Trends Mol. Med. *19*, 302–308.

Fisher, O.S., and Boggon, T.J. (2014). Signaling pathways and the cerebral cavernous malformations proteins: lessons from structural biology. Cell. Mol. Life Sci. *71*, 1881–1892.

Kugelmann, D., Waschke, J., and Radeva, M.Y. (2015). Adducin is involved in endothelial barrier stabilization. PLoS One *10*, e0126213.

Maddaluno, L., Rudini, N., Cuttano, R., Bravi, L., Giampietro, C., Corada, M., Ferrarini, L., Orsenigo, F., Papa, E., Boulday, G., et al. (2013). EndMT contributes to the onset and progression of cerebral cavernous malformations. Nature *498*, 492–496.

Mayor, R., and Etienne-Manneville, S. (2016). The front and rear of collective cell migration. Nat. Rev. Mol. Cell Biol. *17*, 97–109.

McDonald, D.A., Shi, C., Shenkar, R., Stockton, R.A., Liu, F., Ginsberg, M.H., Marchuk, D.A., and Awad, I.A. (2012). Fasudil decreases lesion burden in a murine model of cerebral cavernous malformation disease. Stroke *43*, 571–574.

Pagenstecher, A., Stahl, S., Sure, U., and Felbor, U. (2009). A two-hit mechanism causes cerebral cavernous malformations: complete inactivation of CCM1, CCM2 or CCM3 in affected endothelial cells. Hum. Mol. Genet. *18*, 911–918.

Scarpa, E., and Mayor, R. (2016). Collective cell migration in development. J. Cell Biol. *212*, 143–155.

Schulz, G.B., Wieland, E., Wustehube-Lausch, J., Boulday, G., Moll, I., Tournier-Lasserve, E., and Fischer, A. (2015). Cerebral cavernous malformation-1 protein controls DLL4-Notch3 signaling between the endothelium and pericytes. Stroke *46*, 1337–1343.

Shenkar, R., Shi, C., Rebeiz, T., Stockton, R.A., Mcdonald, D.A., Mikati, A.G., Zhang, L., Austin, C., Akers, A.L., Gallione, C.J., et al. (2015). Exceptional aggressiveness of cerebral cavernous malformation disease associated with PDCD10 mutations. Genet. Med. *17*, 188–196.

Sreenivasappa, H., Chaki, S.P., Lim, S.M., Trzeciakowski, J.P., Davidson, M.W., Rivera, G.M., and Trache, A. (2014). Selective regulation of cytoskeletal tension and cell-matrix adhesion by RhoA and Src. Integr. Biol. (Camb) *6*, 743–754.

Stockton, R.A., Shenkar, R., Awad, I.A., and Ginsberg, M.H. (2010). Cerebral cavernous malformations proteins inhibit Rho kinase to stabilize vascular integrity. J. Exp. Med. *207*, 881–896.

Zhou, Z., Tang, A.T., Wong, W.Y., Bamezai, S., Goddard, L.M., Shenkar, R., Zhou, S., Yang, J., Wright, A.C., Foley, M., et al. (2016). Cerebral cavernous malformations arise from endothelial gain of MEKK3-KLF2/4 signalling. Nature *532*, 122–126.

Zhou, Z.L., Sun, X.X., Ma, J., Tong, M.H., To, S.K.Y., Wong, A.S.T., and Ngan, A.H.W. (2017). Actin cytoskeleton stiffness grades metastatic potential of ovarian carcinoma Hey A8 cells via nanoindentation mapping. J. Biomech. *60*, 219–226.

ISCI, Volume *9*

Supplemental Information

Biomechanics of Endothelial Tubule Formation Differentially Modulated by Cerebral Cavernous Malformation Proteins

Olga Chernaya, Anastasia Zhurikhina, Siarhei Hladyshau, William Pilcher, Katherine M. Young, Jillian Ortner, Vaishnavi Andra, Todd A. Sulchek, and Denis Tsygankov

SUPPLEMENTAL INFORMATION

Supplemental Figures

Figure S1. Related to Figure 1;

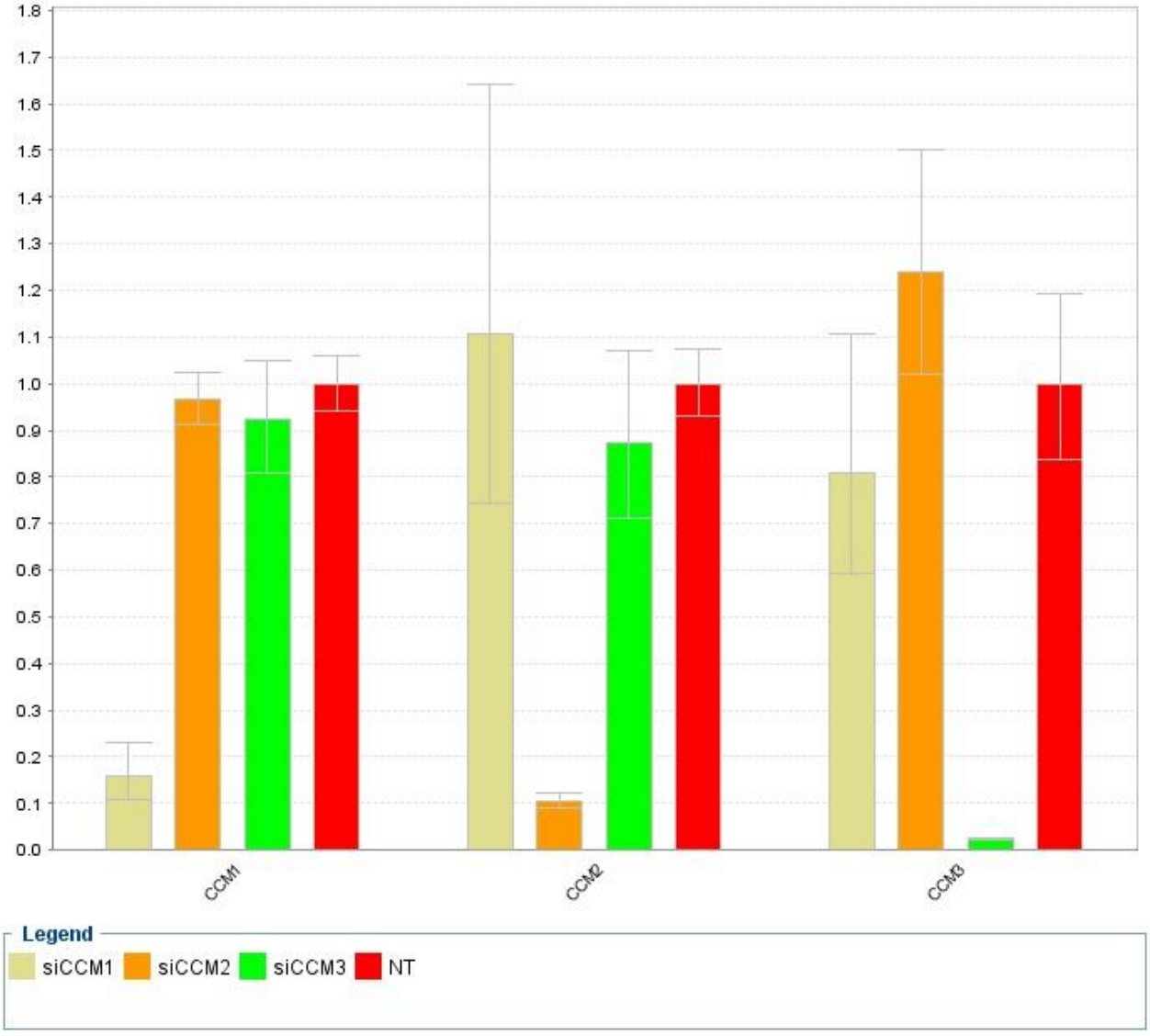

Figure S2. Related to Figure 2;

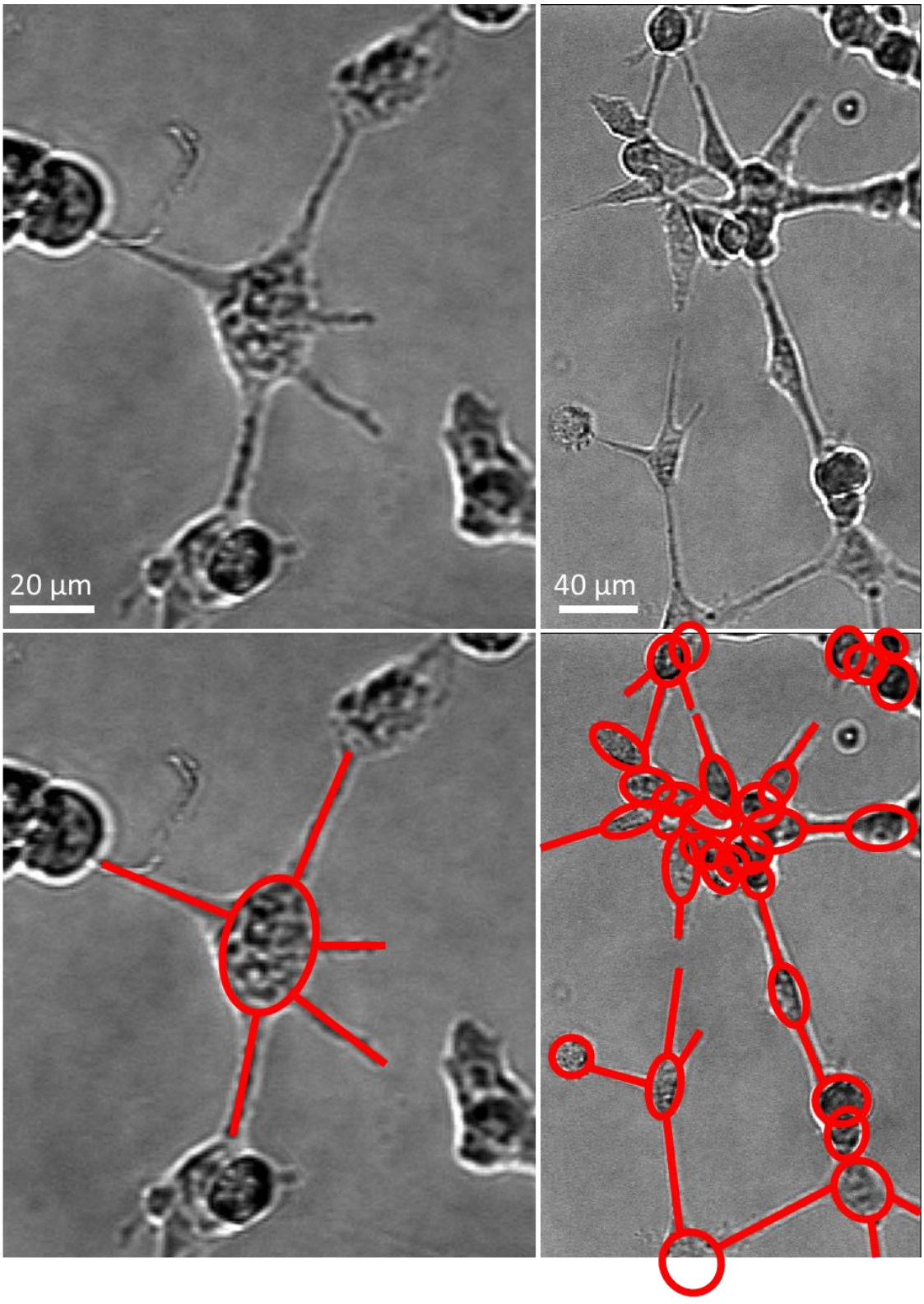

Figure S3. Related to Figure 2;

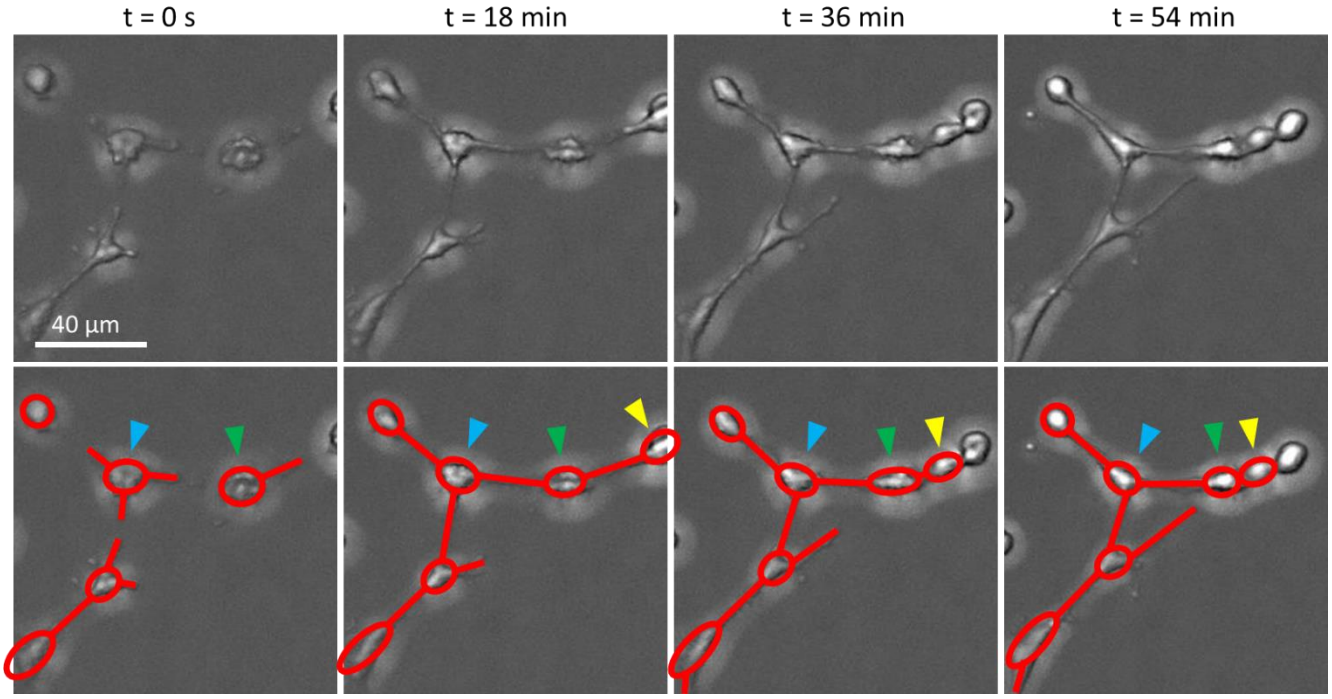

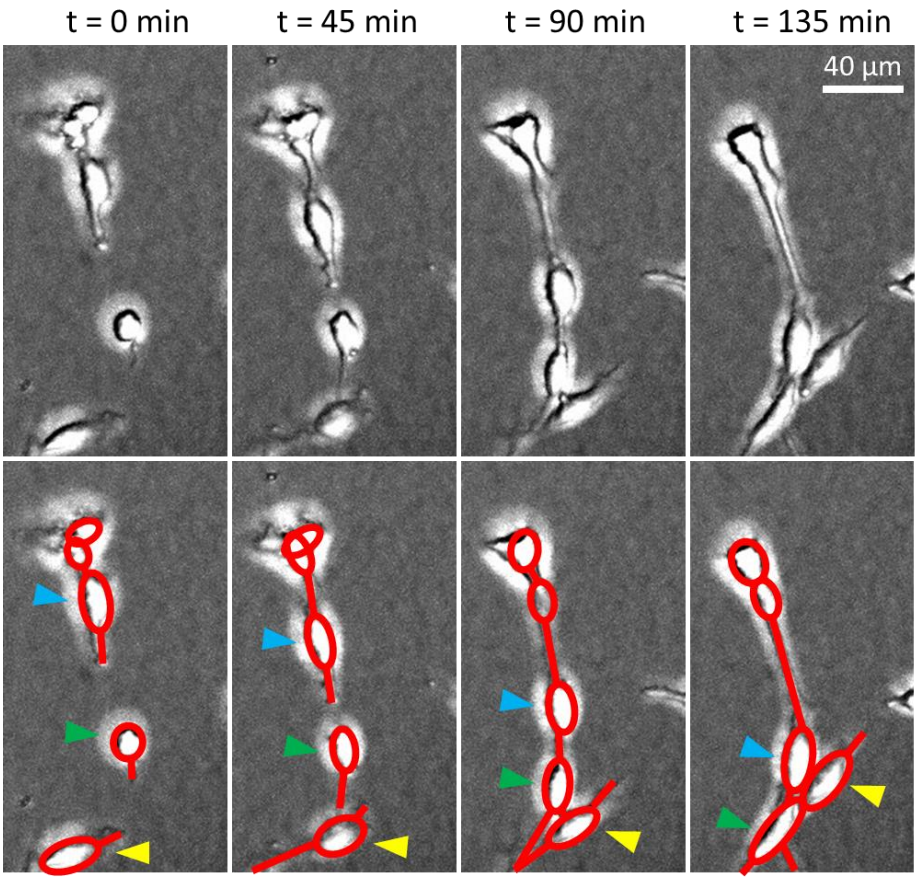

Figure S4. Related to Figure 2;

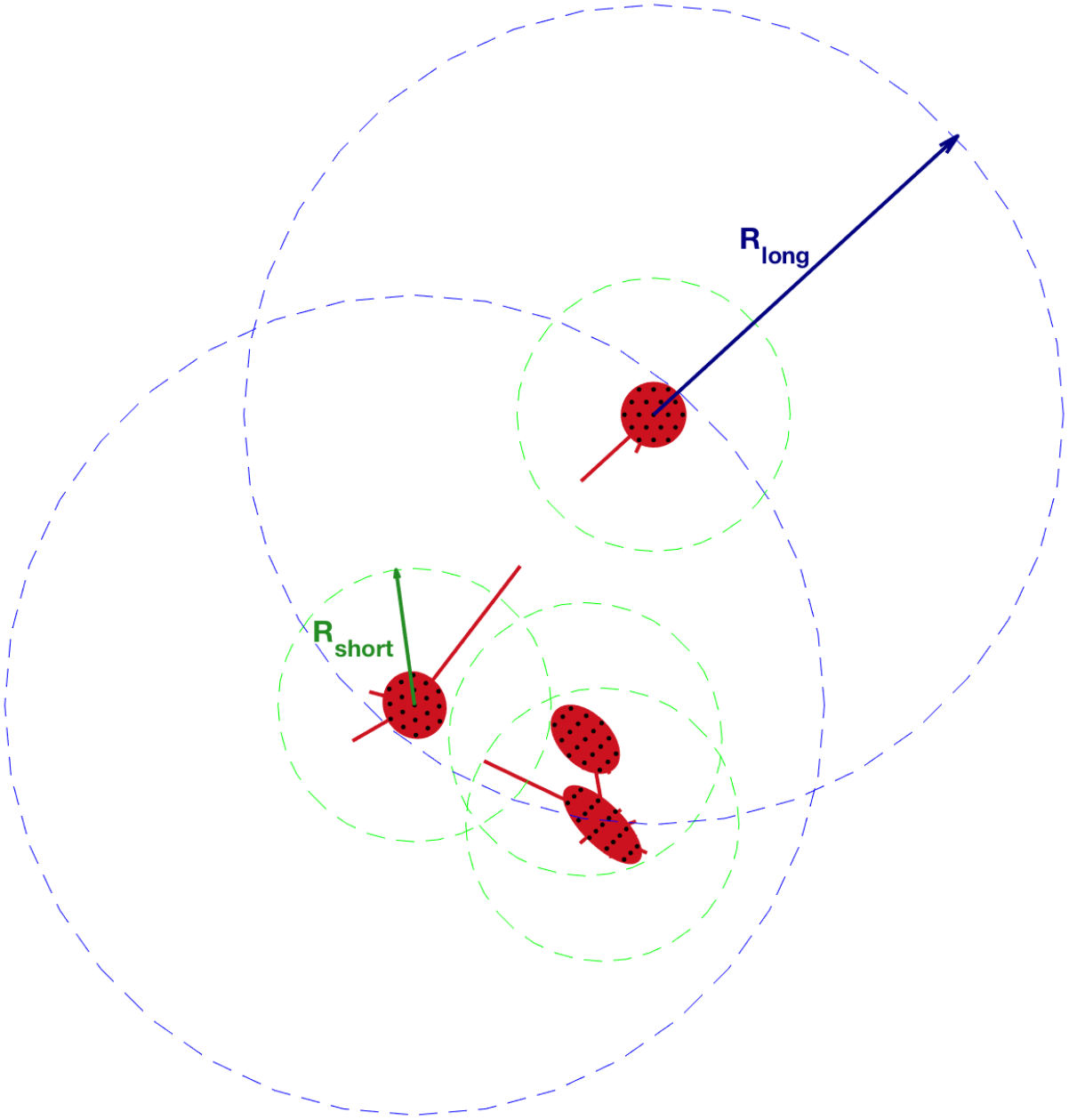

Figure S5. Related to Figure 2;

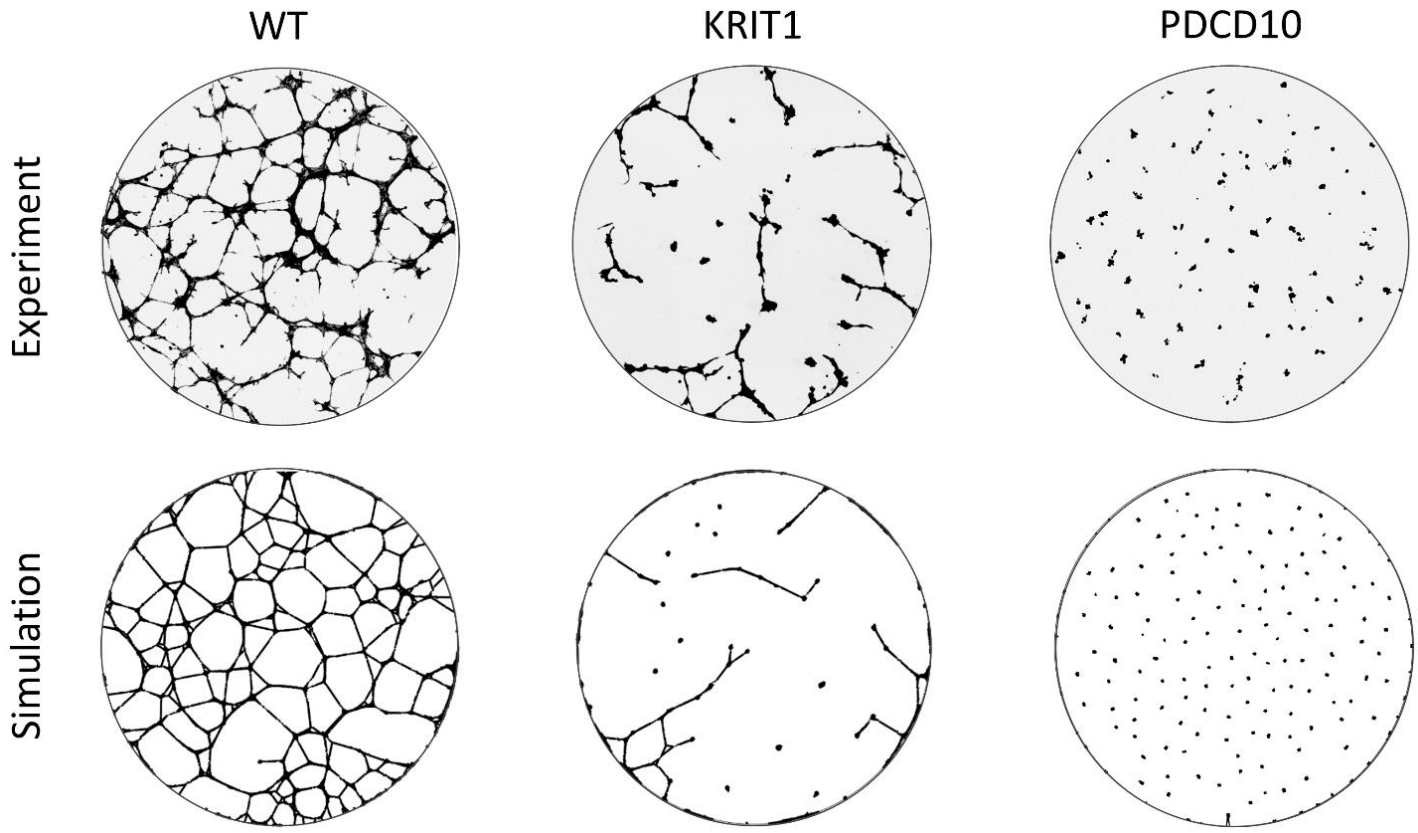

Figure S6. Related to Figure 2;

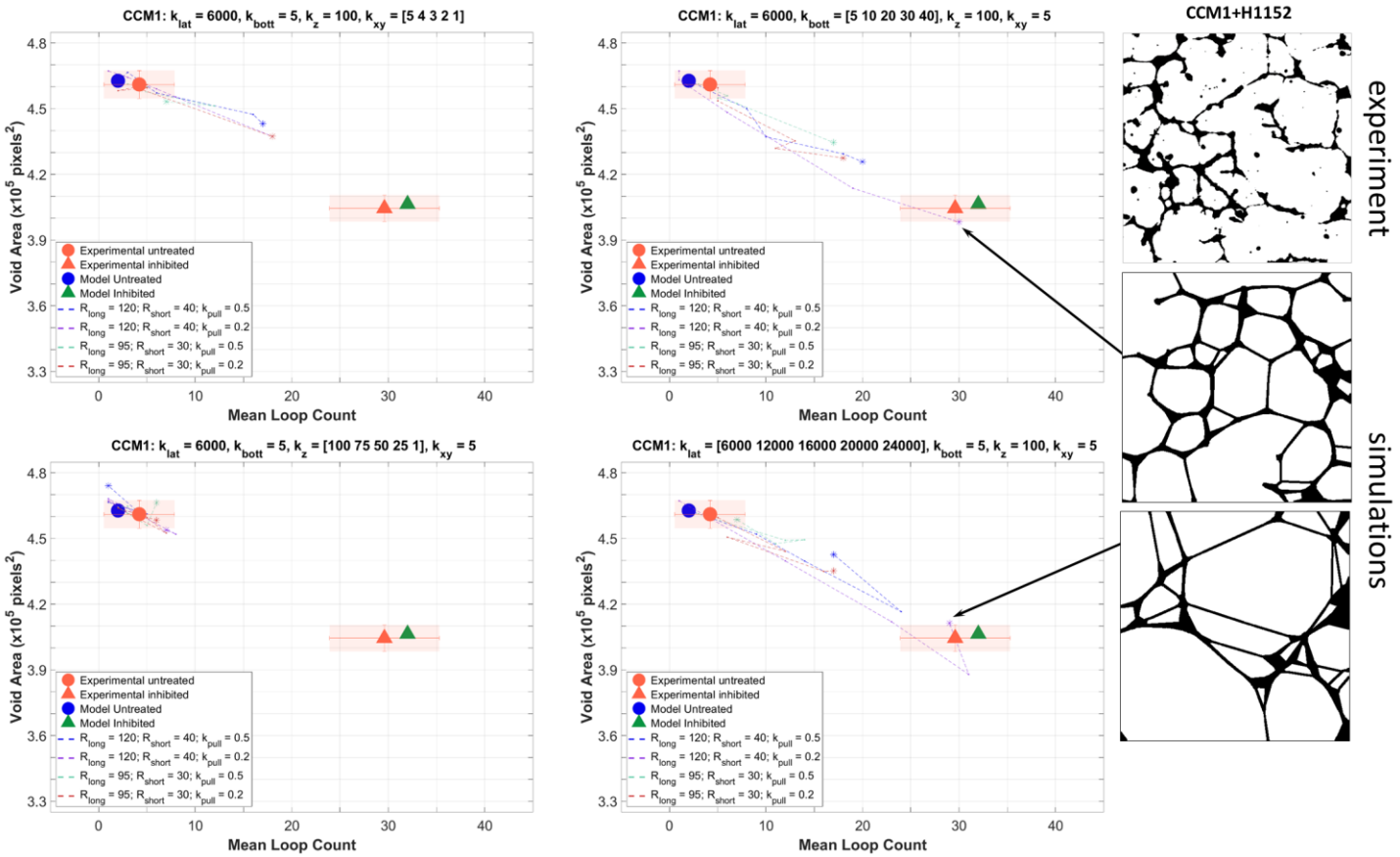

Figure S7

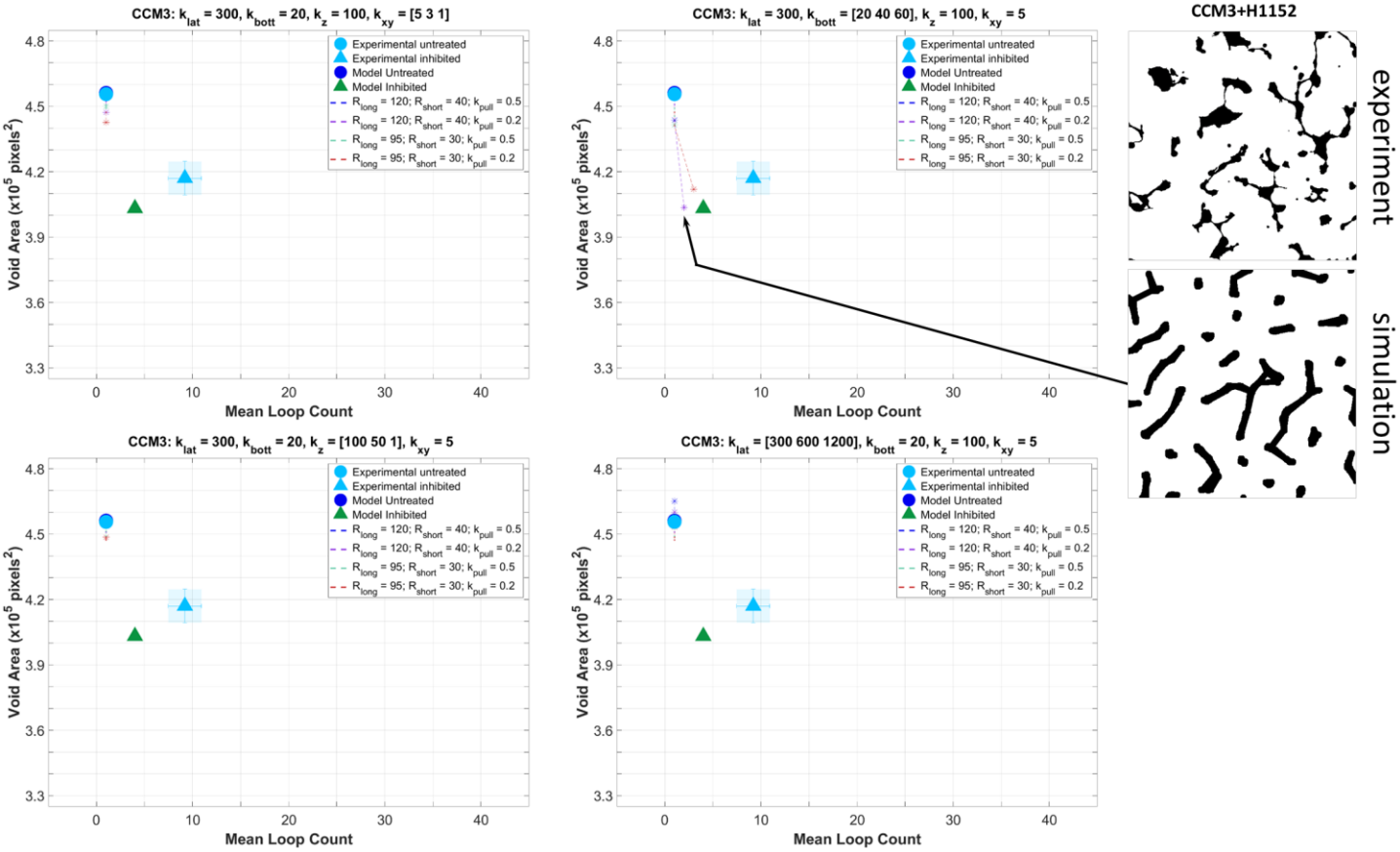

Figure S8. Related to Figure 2;

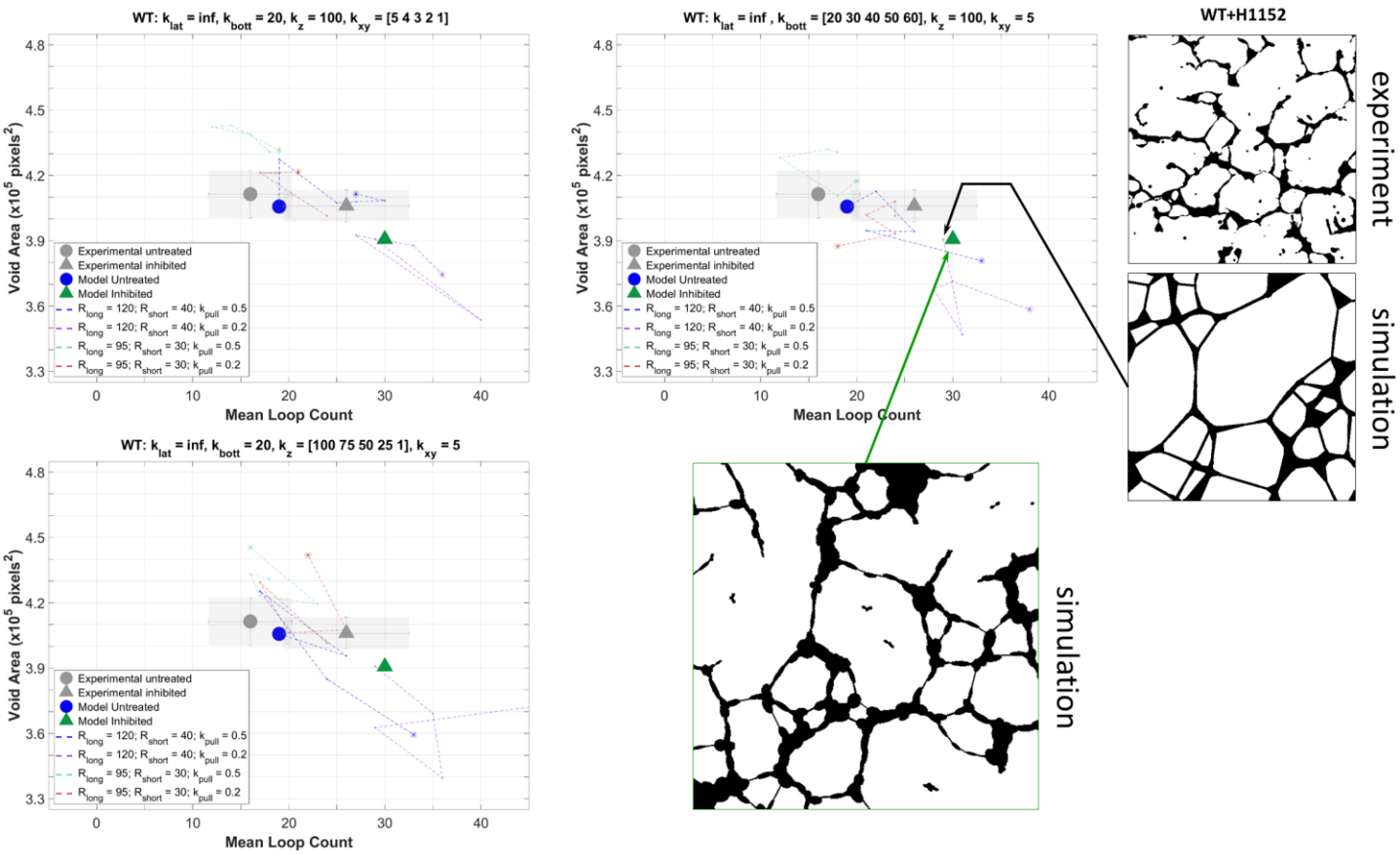

Figure S9. Related to Figure 4;

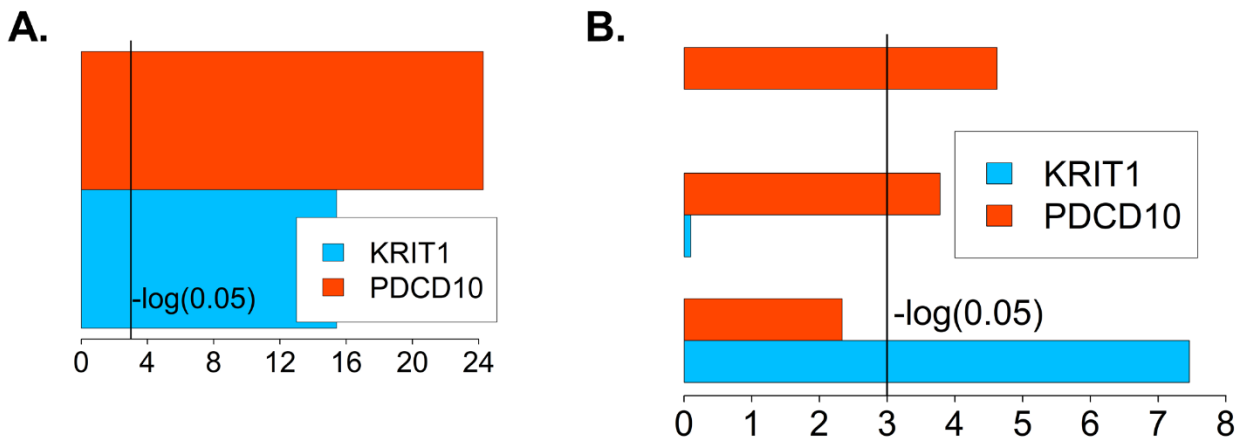

Figure S10. Related to Figure 4;

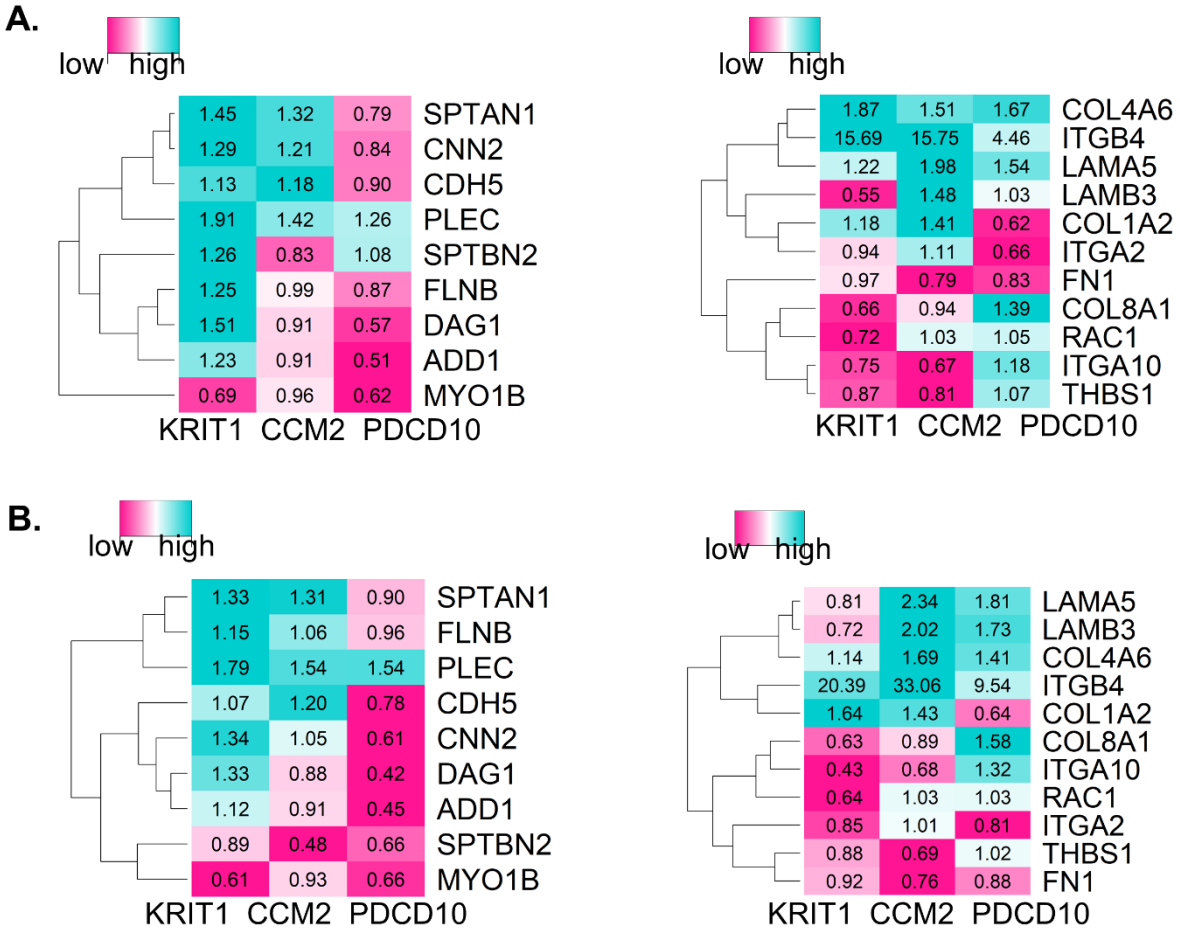

Supplemental Figure Legends

Figure S1: Bar graph demonstrating the efficiency of krit1, ccm2, and pdcd 10 mRNA expression knockdown at 48 hrs after siRNA transfection. Cells were treated as described under Material and Methods. Expression of each gene was analyzed by qPCR, normalized to expression of TBP, and compared to expression in cultures treated with non-target siRNA. The bars represent fold change in mRNA expression (Mean ± SD). Knockdown of expression of any of *ccm* genes did not have an effect on expression levels of the other 2 genes.

Figure S2: Two illustrative examples of cell shapes during the WT endothelial tube formation. In the bottom row, the experimental images from the top row are overplayed with the shapes formed by ellipses (representing cell bodies) and lines (either radially directed 'extending' protrusions or cell-cell attached 'pulling' protrusions). The reasonable accuracy of such simplified shape representation motivated the specifications of cell model in our simulations.

Figure S3: Two illustrative examples of cell shape dynamics during the WT endothelial tube formation. Similar to Figure S2, in the bottom rows in each time series, the experimental images from the top rows are overplayed with the shapes formed by deformable ellipses (representing cell bodies) and lines (either radially directed 'extending' protrusions or cell-cell attached 'pulling' protrusions). Colored arrowheads point to the same cells in each time frame to highlight the extent of cell displacement over the course of time. This dynamics of multicellular interactions through extending and retracting protrusions, which drives the movement and the deformation of cell bodies, motivated the specifications of the cell model in our simulations.

Figure S4: A schematic diagram illustrating the top view (xy-plane) of the cells soon after being platted on Matrigel. Blue and green circles demonstrate the long and short ranges of cell-cell sensing that guides the extension of the corresponding protrusions in the simulation model. Black dots distributed within elliptical cell bodies indicate the vertically directed (z −direction) protrusions, which are responsible for the cell-ECM interaction.

Figure S5: Experimental and simulated patterns of cells initially plated/distributed at equivalent densities (here 1600 cells in the field of view).
Top row: Experimental images of WT, KRIT1, and PDCP10 cell cultures.
Bottom row: Patterns resulted in the simulations of normal and disrupted cell-cell and cell-ECM interactions (same as Figure 2B, but with more cells in the simulations).

Figure S6: Parameter scans for the identification of regimes when void area and mean loop count measures of simulated patterns match the experimental values for KRIT1 KD cells. Experimental values for cultures treated and untreated with ROCK inhibitor (H1152) are shown by orange triangle and circle, respectively. The corresponding values from the simulations reported in the main text of the paper are shown by the green triangle and blue circle. The dash lines in the four graphs show the results from changing one of the parameters ($\kappa_{xy}, \kappa_{lat}, \kappa_z,$ and κ_{bott}) at a time. These results are compared for two regimes of cell-cell sensing (R_{long}, R_{short}) and two regimes of the pulling strength (κ_{pull}). The patterns on the right demonstrate that even when the void area and the mean loop count match experimental values, there are clear differences with regard to other geometric features. However, the trends identified with this scan suggests the combination of parameters that leads to a very close correspondence between the simulated and observed cell patterns (see also Figure 2C)

Figure S7: Parameter scans for the identification of regimes when void area and mean loop count measures of simulated patterns match the experimental values for PDCP10 KD cells. Experimental values for cultures treated and untreated with ROCK inhibitor (H1152) are shown by light blue triangle and circle, respectively. The corresponding values from the simulations reported in the main text of the paper are shown by the green triangle and blue circle. The dash lines in the four graphs show the results from changing one of the parameters ($\kappa_{xy}, \kappa_{lat}, \kappa_z,$ and κ_{bott}) at a time. These results are compared for two regimes of cell-cell sensing (R_{long}, R_{short}) and two regimes of the pulling strength (κ_{pull}). The patterns on the right demonstrate that even when the void area and the mean loop count approach experimental values, there are clear differences with regard to other geometric features. However, the trends identified with this scan suggests the combination of

parameters that leads to a very close correspondence between the simulated and observed cell patterns (see also Figure 2C)

Figure S8: Parameter scans for the identification of regimes when void area and mean loop count measures of simulated patterns match the experimental values for WT cells. Experimental values for cultures treated and untreated with ROCK inhibitor (H1152) are shown by gray triangle and circle, respectively. The corresponding values from the simulations reported in the main text of the paper are shown by the green triangle and blue circle. The dash lines in the four graphs show the results from changing one of the parameters ($\kappa_{xy}, \kappa_z,$ and κ_{bott}) at a time. These results are compared for two regimes of cell-cell sensing (R_{long}, R_{short}) and two regimes of the pulling strength (κ_{pull}). The patterns on the right demonstrate that even when the void area and the mean loop count approach experimental values, there are clear differences with regard to other geometric features. However, the trends identified with this scan suggests the combination of parameters that leads to a very close correspondence between the simulated and observed cell patterns (see also Figure 2C)

Figure S9: Enrichment analysis of differentially expressed genes.
A). Genes associated with cell-cell adhesion in 2D cultures. The graph shows negative log(p-values) for KRIT1 KD cells (blue bars) and PDCD10 cells (red bars) compared to WT cells.
B). Term enrichment for KRIT1 and PDCD10 KD endothelial cells at 2 hours after plating on Matrigel.

Figure S10: Differentially expressed genes involved in cell-cell and cell-ECM adhesion.
A). Heat map of a subset of differentially expressed genes involved in cell-cell (*left*) and cell-ECM (*right*) adhesion in cells cultured under 2D conditions. Text annotation represents fold change of RPKM values in comparison to WT cells.
B). Heat map of a subset of differentially expressed genes involved in cell-cell (*left*) and cell-ECM (*right*) adhesion in cells cultured on Matrigel for 2 hrs.

Supplemental Tables

Table S1. Related to Figure 1B;

P-Values (Void Area)	WT	WT-H1152	CCM1	CCM1-H1152	CCM2	CCM2-H1152	CCM3	CCM3-H1152
WT		0.446672191	0.000227504	0.311436311	0.022358986	0.004723167	0.001329989	0.427082125
WT-H1152	0.446672191		8.92353E-06	0.749524401	0.00334343	0.007518726	0.000180833	0.075260431
CCM1	0.000227504	8.92353E-06		3.91874E-06	0.003510728	7.07116E-05	0.171501257	4.68367E-05
CCM1-H1152	0.311436311	0.749524401	3.91874E-06		0.002820809	0.011538089	8.11118E-05	0.036487194
CCM2	0.022358986	0.00334343	0.003510728	0.002820809		0.000223636	0.012074674	0.038153775
CCM2-H1152	0.004723167	0.007518726	7.07116E-05	0.011538089	0.000223636		0.000233538	0.001642225
CCM3	0.001329989	0.000180833	0.171501257	8.11118E-05	0.012074674	0.000233538		0.000579579
CCM3-H1152	0.427082125	0.075260431	4.68367E-05	0.036487194	0.038153775	0.001642225	0.000579579	

P-Values (Mean Loop Count)	WT	WT-H1152	CCM1	CCM1-H1152	CCM2	CCM2-H1152	CCM3	CCM3-H1152
WT		0.043594134	0.004233614	0.006651511	0.207586693	0.008019723	0.002289809	0.033187737
WT-H1152	0.043594134		0.001133036	0.433314131	0.010062099	0.769664482	0.001574521	0.007667694
CCM1	0.004233614	0.001133036		0.000285754	0.021079927	8.14552E-05	0.154842121	0.056159092
CCM1-H1152	0.006651511	0.433314131	0.000285754		0.002106554	0.522263806	0.000546202	0.002342745
CCM2	0.207586693	0.010062099	0.021079927	0.002106554		0.001129274	0.004401545	0.236695303
CCM2-H1152	0.008019723	0.769664482	8.14552E-05	0.522263806	0.001129274		0.000262217	0.0005683
CCM3	0.002289809	0.001574521	0.154842121	0.000546202	0.004401545	0.000262217		0.000676315
CCM3-H1152	0.033187737	0.007667694	0.056159092	0.002342745	0.236695303	0.0005683	0.000676315	

Table S2. Related to Figure 2;

Main model Parameters/Constants			
Parameter Name	**Parameter description**	**Value**	**Units**
κ_{lat}	A constant defining the probability of cell-ECM contacts breakage: $P_{\text{cell-cell}} = 1 - \exp(-l^2/k_{lat}^2)$	∞ (WT); 6000 (CCM1); 300 (CCM3)	μm
κ_{bott}	A constant defining the probability of cell-ECM contacts breakage: $P_{\text{cell-ECM}} = 1 - \exp(-l^2/k_{bott}^2)$	20 (WT); 5 (CCM1); 20 (CCM3)	μm
κ_z	Spring constant representing cytoskeletal resistance to vertical deformations (spreading)	100 · S	N/m
κ_{xy}	Spring constant representing cytoskeletal resistance to in-plane deformations (stretching)	5 · S	N/m
κ_{pull}	Spring constant of cell-cell and cell-ECM contact	0.5 · S	N/m
R_{long}	The maximal extent of long-range protrusions (the range of cell-cell sensing)	120	μm
R_{short}	The maximal extent of short-range protrusions	40	μm
R_{bott}	The attachment range of ventral protrusions	2.6	μm
N_{bott}	The maximal number of bottom protrusions	19	1
N_{long}	The maximal number of long-range protrusions	5	1
N_{lim}	The limit on the number of extending protrusions	15	1
$u_{prot}\ (lateral)$	Growth rate of lateral protrusions in the 'extending' mode	0.017	μm /s
$u_{prot}\ (bottom)$	Growth rate of ventral protrusions in the 'extending' mode	0.003	μm /s
u_{retr}	Retraction rate of lateral protrusions in the 'pulling' mode	0.003	μm /s
η_{xy}	Viscous drag in response to *x* and *y* displacement	0.4 · S	N*s/m
η_{ab}	Viscous drag in response to cell body elongation	20 · S	N*s/m
η_{φ}	Viscous drag in response to cell rotation (in *xy*-plane)	0.13 · S	N*s/m
η_{ξ}	Viscous drag in response to the shift of protrusions bases with respect to the semi-principle axes (in *xy*-plane)	0.6 · S	N*s/m
R_0	Mean radius of individual cells	6.32	μm
R_{box}	Dish radius (simulation domain)	863 (Figs. 2); 1600 (S.Fig. 3)	μm
N	Total number of cells	466 (Figs. 2); 1600 (S.Fig. 3)	1
D	Density of cells per plating area	0.0002 $(N/\pi R_{box}^2)$	1/μm^2
S	Arbitrary scaling parameter	-	unitless

Table S3. Related to Figure 4;

WT /2D	KRIT1 /2D	CCM2 /2D	PDCD10 /2D
WT /3D-2hrs	KRIT1 /3D-2hrs	CCM2 /3D-2hrs	PDCD10 /3D-2hrs
WT /3D-6hrs	KRIT1 /3D-6hrs	CCM2 /3D-6hrs	PDCD10 /3D-6hrs

Supplemental Table Legends

Table S1: Comparison of Void area and Mean loop count in untreated and treated with ROCK inhibitor WT and KD cells.
Green: $p \leq 0.05$ for pair-wise comparison in Student's t-test
Red: $p > 0.05$ for pair-wise comparison in Student's t-test.

Table S2. Model parameters.
Green: parameters defining cell-cell and cell-matrix interactions
Yellow: parameters defining protrusion and retraction rates
Orange: force-velocity coefficients for the system's coordinates
Blue: parameters defining cell size, number, and the simulation domain.

Table S3: Genotypes and cell cultures conditions analyzed by RNA-sequencing.

Transparent Methods

Cell culture

Human umbilical cord endothelial cells HUVEC (Lonza, Walkersville, MD) were maintained in EGM-2 medium (Lonza) at 37°C/5% CO_2 and passaged every 3 to 4 days for up to 6 passages at a 1:5 sub-culturing ratio. For tube formation experiments, 4.5-5x10^3 cells were plated into each well of angiogenesis µ-slides (ibidi, Fitchburg, WI) coated with 10 µl of growth factor reduced phenol red-free Matrigel (Corning, Corning, NY), and incubated for up to 18 hrs.

Microscopy

Cells plated on Matrigel-coated glass coverslips were fixed in 4% para-formaldehyde for 10 min, permeabilized with 0.1% Triton X100/PBS for 5 min. Actin filaments were stained with rhodamine-phalloidin (Molecular Probes, Carlsbad, CA), and nuclei were counterstained with DAPI (Molecular Probes, Carlsbad, CA). The cells were imaged using a Zeiss LSM 700 confocal microscope.
For time-lapse imaging of endothelial tubule formation, cells plated on Matrigel were incubated with CellMask™ Green Plasma Membrane Stain (Invitrogen, Carlsbad, CA) for 15 min at 37°C, the media was changed to phenol-free EGM-2 supplemented with 2% FBS and growth factors (PromoCell GmbH). Images were acquired using PerkinElmer UltraVIEW VoX spinning disk confocal microscope (PerkinElmer, Waltham, MA). Image processing and analysis were performed using ImageJ software (NIH).

Gene expression knockdown

To achieve knockdown of CCM protein expression, cells were infected with PLKO.1 vector based lentiviruses carrying shRNAs for human *krit1* (RHS4533-EG889), *ccm2* (RMM4534-EG216527), and *pdcd10* (RHS4533-EG11235) genes (Dharmacon, Lafayette, CO). Lentiviral particles, prepared and purified by VectorBuilder technical service group (VectorBuilder, Santa Clara, CA) were added to EGM-2 media supplemented with 8µ/mL polybrene for 48 hrs. Transduced cells were selected through their resistance to puromycin added to the growth media in the concentration of 2.5 µg/ml. Expression knockdown was measured by real-time PCR with TaqMan gene expression assays. Phenotypic experiments were conducted between 6 and 10 days after infection.
Where indicated, cells were transfected with 50 nM siRNA against human *krit1* (LQ-003825-00), *ccm2* (LG-014728-01), and *pdcd10* (LQ-004436-00), or control non-targeting siRNA (D-001810-01-05), using DharmaFECT 4 transfection reagent (all from Dharmacon, Lafayette, CO). Gene expression was analyzed at 48 hrs, protein expression at 72 hrs after transfection, and phenotypic studies were conducted 60-72 hrs after transfection.

Real-time PCR

Total RNA was extracted using RNeasy extraction kit (Qiagen, Valencia, CA, USA) following the manufacturer's protocol. RNA was reverse-transcribed using the high-capacity cDNA kit (Life Technologies, Carlsbad, CA, USA). The analysis was done StepOnePlus™ Real-Time PCR System (Applied Biosystems, Foster City, CA), and the level of transcripts was quantified using TaqMan probes (Applied Biosystems): KRIT1 Hs01090981_m1; CCM2 Hs01123856_m1; PDCD10 Hs00200578_m1; TBP Hs00427620_m1. Fold change in gene expression was determined using $\Delta\Delta C_t$ algorithm.

Adhesion assay

Adhesion assays were performed in 96-well plates coated with growth factor-reduced Matrigel. 1x10^4 cells were plated in each well, and allowed to attach for 30 min at 37°C. To remove non-adherent cells, growth media was replaced and the adherent cells were incubated for additional 2 hrs in fresh media containing 20 µl of 5 mg/mL of Thiazolyl Blue Tetrazolium Bromide, MTT (Sigma-Aldrich, St. Louis, MO). Following incubation, the cells were lysed in 10% Triton X100 in acidic isopropanol, and an absorbance at 590 nm was determined.

Western Blotting

Cells were lysed in RIPA buffer supplemented with protease inhibitor cocktail, sonicated briefly, and cleared by centrifugation and boiled in Laemmli SDS sample buffer. 10 µg of protein per lane was separated by SDS-PAGE and transferred to nitrocellulose membranes. Membranes were blocked and incubated overnight at +4°C with primary antibodies against KRIT1, CCM2, PDCD10, phosphorylated myosin light chain (ThermoFisher Scientific, Rockford, IL) phosphorylated cofilin, and actin (Novus Biologicals, Littleton, CO). Next, membranes were incubated with HRP-conjugated secondary antibodies (all from ThermoFisher Scientific, Rockford, IL), and developed using West Pico PLUS chemiluminescent substrate (ThermoFisher Scientific, Rockford, IL).

RNA sequencing

HUVEC cells were transfected with non-targeting siRNA or siRNA against *krit1*, *ccm2*, and *pdcd10* genes as described above. 48 hrs after transfection cells were plated on growth factor reduced Matrigel, and incubated for 2 hrs (initial stages of endothelial tubule formation) or 6 hrs (advanced stages of tubule formation). Total RNA was isolated from each culture (control, and siRNA against *krit1*, *ccm2*, and *pdcd10*) cells cultured on the 2D (Matrigel-coated plastic), and in 3D (Matrigel) substrate, using RNAeasy kit (Qiagen, Valencia, CA, USA) per the manufacturer's instructions. RNA quality control was performed by studying the relative intensity of 18s and 28s rRNA bands using an Agilent 2100 Bioanalyzer and RNA6000 Pico LabChip Kit (Agilent Technologies). Between 200ng and 1ug of RNA were used directly in the TruSeq mRNA stranded kit (Illumina, San Diego, CA) for isolation of mRNA from total RNA, generation of ds cDNA and preparation of libraries. The cDNA was quantified using the Qubit HS DNA kit (Thermo Fisher Scientific, Rockford, IL), and cDNA libraries were prepared using a TruSeq Stranded mRNA library prep kit (Illumina, San Diego, CA). The samples were run on a NextSeq 550 instrument (Illumina, San Diego, CA) with a read length of PE75bp.

RNA-seq analysis

RNA-Seq analysis for 12 conditions (knockouts of KRIT1, CCM2, PDCD10 and non-targeted RNA interference, for cells cultured on 2D surface and in 3D gels for 2 and 6 hours) was performed using raw reads from Illumina NextSeq 550 machine (paired-end reads, 75 bp). BBDuk, BBTools package Version 35.92 [BBMap - Bushnell B. - sourceforge.net/projects/bbmap/] was used for quality control and adapter trimming; TopHat2 v2.1.1 (Kim et al., 2013) was used for transcriptome alignment (Srinivasan et al., 2017). RNA-Seq reads were mapped against the human genome build GRCh38 (Cunningham et al., 2015). We applied GFOLD algorithm (Feng et al., 2012) for biologically meaningful rankings of differentially expressed genes, samples with knockouts were compared with non-targeted RNA interference, and a value of 0.3 was used as a cutoff for generalized fold change. Visualization of gene expression was performed with custom R script. For quantification of pathways enrichment we used David Web Services v6.8 (https://david.ncifcrf.gov/).

Atomic Force Microscopy

Adherent cells were grown on glass FluoroDishes (World Precision Instruments, Sarasota, FL) at 37°C before stiffness measurements were taken. For better global stiffness measurements of the cell, 5.46 µm spherical polystyrene particles were attached to tipless silica nitride cantilevers (MLCT-O10 Bruker Probes, Camarillo, CA) using a two-part epoxy and dried for at least 24 hours. To characterize the mechanical properties of each cell, we used force spectroscopy to obtain force-indentation curves with an atomic force microscope (Asylum Research, Santa Barbara, CA) with an integrated optical microscope (Nikon, Melville, NY) on a vibration isolation table.

Before each day of measurements, the AFM was calibrated by taking a single force curve on a clean FluoroDish to determine the deflection inverse optical lever sensitivity for the particular cantilever. The force exerted on the cell is calculated using Hooke's law which states that $F = k \cdot \Delta x$, using the spring constant found during calibration and the cantilever deflection. For measurements, the cantilever probe was visually aligned with the cell center and moved with a velocity of 2 µm/s to indent the cell with increasing compressive force until a force trigger of 10 nN was reached, completing the approach portion of the force curve, at which point the probe would reverse the direction of its velocity to create the retraction portion of the force curve.

The Hertzian contact model was used to calculate the cellular Young's modulus. The model was fit to the approach or compression segment of the force-indentation curve between 10-90% of the curve where Young's

modulus was independent of indentation. The cells were assumed to be incompressible so that the Poisson's ratio was input into the model as 0.5. We took one measurement per cell and probed 30-50 cells per cell type.

Quantitative Image Analysis of F-actin distribution

For the analysis of the "percent of active area" we quantified the presence of non-contractile actin network at the cell edge. To do this, we subtracted MLC channel from the F-actin channel (both thresholded to eliminate the background fluorescence) for each images cell. Part of the image with co-localized F-actin bindles and MLC cancels out, while the remaining non-zero signal indicates the non-bundled F-actin. In Figure 3 we report the ratio of the area (sum of non-zero pixels) occupied by this non-bundled F-actin within a peripheral strip of 50 pixels (4.3μm) to the total area (sum of both zero and non-zero pixel) of the strip.
For the analysis of the internal distribution of F-actin bundles, we perform the standard texture quantification using the "Contrast" and "Homogeneity" measures. To this end, we constructed the gray-level co-occurrence matrix $p(i,j)$ from each cell image using 8 gray-levels, symmetric ordering, and four offsets in 0, 45, 90, and 135-degree directions. The contrast and homogeneity are defined as $\sum_{i,j}|i-j|^2 p(i,j)$ and $\sum_{i,j}\frac{p(i,j)}{1+|i+j|}$, respectively. In Figure 3, we report the results for the offset distance of 20 pixels (1.72 μm) averaged over the four offset directions. However, the conclusion regarding the significance of the differences in contrast and homogeneity are not sensitive to a choice of the number of gray-levels or the size of the offset.

Quantitative Image Analysis of multicellular formations

A binary mask of the cell formation was formed with a uniform intensity threshold on each field, followed by a manual correction to add back any low-intensity connections that were removed by thresholding but still clearly visible by eye. Small holes in the cellular network from noise or over-thresholding in dimmer areas were filled by a flood-fill operation. Isolated cell objects in the background from the cellular debris were also removed with an area filter. Two features, void area and hole count, were derived from each binary mask through a custom MATLAB script. Void area is the number of pixels belonging to the background in each mask. Holes were defined as continuous regions in the background not divided by cells, tubules, or the image border. The Mean loop count represents the number of these isolated regions in each image. The mean and standard error of these measures were computed for each condition.

Statistical Analysis

Results are expressed as mean ± 2 standard errors unless stated otherwise. Comparisons between groups were analyzed by t-tests. P values <0.05 were considered as statistically significant.

Supplemental References

CUNNINGHAM, F., AMODE, M. R., BARRELL, D., BEAL, K., BILLIS, K., BRENT, S., CARVALHO-SILVA, D., CLAPHAM, P., COATES, G., FITZGERALD, S., GIL, L., GIRON, C. G., GORDON, L., HOURLIER, T., HUNT, S. E., JANACEK, S. H., JOHNSON, N., JUETTEMANN, T., KAHARI, A. K., KEENAN, S., MARTIN, F. J., MAUREL, T., MCLAREN, W., MURPHY, D. N., NAG, R., OVERDUIN, B., PARKER, A., PATRICIO, M., PERRY, E., PIGNATELLI, M., RIAT, H. S., SHEPPARD, D., TAYLOR, K., THORMANN, A., VULLO, A., WILDER, S. P., ZADISSA, A., AKEN, B. L., BIRNEY, E., HARROW, J., KINSELLA, R., MUFFATO, M., RUFFIER, M., SEARLE, S. M., SPUDICH, G., TREVANION, S. J., YATES, A., ZERBINO, D. R. & FLICEK, P. (2015). Ensembl 2015. *Nucleic Acids Res,* 43**,** D662-9.

FENG, J., MEYER, C. A., WANG, Q., LIU, J. S., SHIRLEY LIU, X. & ZHANG, Y. (2012). GFOLD: a generalized fold change for ranking differentially expressed genes from RNA-seq data. *Bioinformatics,* 28**,** 2782-8.

KIM, D., PERTEA, G., TRAPNELL, C., PIMENTEL, H., KELLEY, R. & SALZBERG, S. L. (2013). TopHat2: accurate alignment of transcriptomes in the presence of insertions, deletions and gene fusions. *Genome Biol,* 14**,** R36.

SRINIVASAN, S., SU, M., RAVISHANKAR, S., MOORE, J., HEAD, P., DIXON, J. B. & VANNBERG, F. (2017). TLR-exosomes exhibit distinct kinetics and effector function. *Sci Rep,* 7**,** 41623.